A&A 669, A137 (2023)
https://doi.org/10.1051/0004-6361/202244183

Astronomy & Astrophysics

PRODIGE – envelope to disk with NOEMA

II. Small-scale temperature structure and streamer feeding the SVS13A protobinary based on CH_3CN and DCN⋆

T.-H. Hsieh[1], D. M. Segura-Cox[2,1,⋆⋆], J. E. Pineda[1], P. Caselli[1], L. Bouscasse[3], R. Neri[3], A. Lopez-Sepulcre[3,4], M. T. Valdivia-Mena[1], M. J. Maureira[1], Th. Henning[5], G. V. Smirnov-Pinchukov[5], D. Semenov[5], Th. Möller[6], N. Cunningham[4], A. Fuente[7], S. Marino[8,9], A. Dutrey[10], M. Tafalla[7], E. Chapillon[3,10], C. Ceccarelli[4], and B. Zhao[11]

[1] Max-Planck-Institut für extraterrestrische Physik, Giessenbachstrasse 1, 85748 Garching, Germany
e-mail: thhsieh@mpe.mpg.de
[2] Department of Astronomy, The University of Texas at Austin, 2515 Speedway, Austin, TX 78712, USA
[3] Institut de Radioastronomie Millimétrique (IRAM), 300 rue de la Piscine, 38406, Saint-Martin d'Hères, France
[4] IPAG, Université Grenoble Alpes, CNRS, 38000 Grenoble, France
[5] Max-Planck-Institut für Astronomie, Königstuhl 17, 69117 Heidelberg, Germany
[6] I. Physikalisches Institut, Universität zu Köln, Zülpicher Str. 77, 50937 Köln, Germany
[7] Observatorio Astronómico Nacional (IGN), Alfonso XII 3, 28014 Madrid, Spain
[8] Jesus College, University of Cambridge, Jesus Lane, Cambridge CB5 8BL, UK
[9] Institute of Astronomy, University of Cambridge, Madingley Road, Cambridge CB3 0HA, UK
[10] Laboratoire d'Astrophysique de Bordeaux, Université de Bordeaux, CNRS, B18N, Allée Geoffroy Saint-Hilaire, 33615 Pessac, France
[11] Department of Physics and Astronomy, McMaster University, Hamilton, ON L8S 4E8, Canada

Received 3 June 2022 / Accepted 7 November 2022

ABSTRACT

Aims. We present high-sensitivity and high spectral-resolution NOEMA observations of the Class 0/I binary system SVS13A, composed of the low-mass protostars VLA4A and VLA4B, with a separation of ∼90 au. VLA4A is undergoing an accretion burst that is enriching the chemistry of the surrounding gas, which provides an excellent opportunity to probe the chemical and physical conditions as well as the accretion process.
Methods. We observe the (12_K–11_K) lines of CH_3CN and $CH_3{}^{13}CN$, the DCN (3–2) line, and the $C^{18}O$ (2–1) line toward SVS13A using NOEMA.
Results. We find complex line profiles at disk scales that cannot be explained by a single component or pure Keplerian motion. By adopting two velocity components to model the complex line profiles, we find that the temperatures and densities are significantly different among these two components. This suggests that the physical conditions of the emitting gas traced via CH_3CN can change dramatically within the circumbinary disk. In addition, combining our observations of DCN (3–2) with previous ALMA observations at high angular resolution, we find that the binary system (or VLA4A) might be fed by an infalling streamer from envelope scales (∼700 au). If this is the case, this streamer contributes to the accretion of material onto the system at a rate of at least $1.4 \times 10^{-6}\ M_\odot\ \mathrm{yr}^{-1}$.
Conclusions. We conclude that the CH_3CN emission in SVS13A traces hot gas from a complex structure. This complexity might be affected by a streamer that is possibly infalling and funneling material into the central region.

Key words. astrochemistry – binaries: close – stars: formation – ISM: kinematics and dynamics

1. Introduction

The discovery of complex organic molecules (COMs, i.e., C-bearing molecules containing ≥6 atoms, Herbst & van Dishoeck 2009) in high-mass star-forming regions has led to the finding that these COMs are sublimated from the icy mantles into the gas-phase in the hot (≥100 K) and dense ($\geq 10^7\ \mathrm{cm}^{-3}$) regions heated by the central source. These molecules are also present in chemically rich cores and disks (Caselli & Ceccarelli 2012; van Dishoeck 2014, and references therein). In low-mass star-forming regions, the COM emission is confined in a compact region with $T \geq 100$ K surrounding the protostar and it is called "hot corino" (Ceccarelli 2004). In these environments, COMs are believed to be at least partially released from the icy mantles due to thermal evaporation and also formed in the gas phase upon sublimation of parent species. However, it has also been suggested that such COM emission can trace accretion shocks, disk atmospheres, or outflow cavities (Drozdovskaya et al. 2015; Csengeri et al. 2018; Belloche et al. 2020). It is therefore important to study these objects and their surroundings in detail to unveil their nature.

⋆ Based on observations carried out under project number L19MB with the IRAM NOEMA Interferometer. IRAM is supported by INSU/CNRS (France), MPG (Germany) and IGN (Spain).
⋆⋆ NSF Astronomy and Astrophysics Postdoctoral Fellow.

The symmetric top CH_3CN molecule, with its K-ladder transitions, provides a powerful tool for diagnosing the temperature structure in hot dense regions and it is commonly observed in high-mass star-forming regions (Galván-Madrid et al. 2010; Beltrán et al. 2011; Hunter et al. 2014; Ilee et al. 2016). In low-mass star-forming regions, CH_3CN has been detected in NGC 1333 IRAS4B/2A (Bottinelli et al. 2007), IRAS 16293-2422 (Bisschop et al. 2008; Calcutt et al. 2018), as well as in several sources from the CALYPSO (Belloche et al. 2020) and PEACHES surveys (Yang et al. 2021). In addition, with high angular-resolution observations, CH_3CN has been found to directly trace the Class II disk surfaces in recent works (Bergner et al. 2018; Loomis et al. 2018).

SVS13 is a multiple system located in the NGC 1333 cluster within the Perseus molecular cloud complex (d = 293 pc, Ortiz-León et al. 2018). The multiple system includes a Class I close binary SVS13A (VLA 4A/B or Per-emb-44B/A), with a separation of 0.″3 (~90 au) and three companions at a distance of 5.″3 (SVS13A2, ~1600 au), 14.″9 (SVS13B, ~4400 au), and 34.″5 (SVS13C, ~10 000 au) based on continuum emission (Anglada et al. 2004; Tobin et al. 2016, 2018; Segura-Cox et al. 2018; Tychoniec et al. 2020). The close binary drives multiple jets and outflows (Lefèvre et al. 2017; Lee et al. 2016; Stephens et al. 2018), and the presence of jet wiggling suggests that an extra undetected source may be present (~20–30 au from VLA4B, Lefèvre et al. 2017). A dusty tail or spiral at 1.3 mm is seen connected to VLA4A (Tobin et al. 2018), suggested to be a fragmenting disk based on its gravitational instability. Recently, with the Atacama Large Millimeter Array (ALMA) 0.9 mm observations at high angular resolution (0.″1 or ~30 au), Diaz-Rodriguez et al. (2022) found a circumbinary disk, as well as two circumstellar disks, around VLA4A/B. These authors estimated the stellar masses using orbital motions (see also Maureira et al. 2020 for a similar method on the Class 0 binary IRAS 16293A). The total mass of the binary was found to be 1.0±0.4 $M_\odot$ and the masses of the individual protostars were estimated as 0.27±0.10 $M_\odot$ for VLA4A and 0.60±0.20 $M_\odot$ for VLA4B. In addition, SVS13A is considered to be a protostar system undergoing an accretion burst, given the high bolometric luminosity, L_{bol} = 45.3 $L_\odot$ (Hsieh et al. 2019). The origin of such accretion outbursts are still unclear (Audard et al. 2014), however, they may be triggered by gravitational instability (Vorobyov & Basu 2010) or magnetorotational instability (Armitage et al. 2001). In addition, anisotropic envelope accretion could also lead to bursts. Indeed, recent observations have found infalling streamers at envelope scales, which have also been suggested to change the protostellar accretion by funneling material into the inner region (Pineda et al. 2020, 2022; Alves et al. 2020; Ginski et al. 2021; Murillo et al. 2022; Cabedo et al. 2021; Garufi et al. 2022; Thieme et al. 2022; Valdivia-Mena et al. 2022). Such infalling streamers are also found in numerical simulations (Seifried et al. 2015; Seifried & Walch 2015; Zhao et al. 2018).

Regarding the chemical complexity, a large number of COMs have been detected toward SVS13A (De Simone et al. 2017; Belloche et al. 2020; Yang et al. 2021). For instance, water emission was detected with a broad linewidth ~5–20 km s^{-1} (NGC 1333-IRAS3A; Kristensen et al. 2012). Using the IRAM 30 m telescope, Codella et al. (2016) detected deuterated water (HDO) emission toward SVS13A, and a non-local thermal equilibrium (non-LTE) analysis has suggested that it comes from a hot (150–260 K), dense (≥3 × 10^7 cm^{-3}), and compact (R ~ 25 au) region. Given such physical conditions, it has been suggested that the COM emission comes from a hot corino inside SVS13A. Diaz-Rodriguez et al. (2022) have found a circumstellar disk around VLA4A, with a radius of ~30 au traced by ethylene glycol (aGg'-$(CH_2OH)_2$). Furthermore, Bianchi et al. (2017, 2019) found that the COM abundances are not significantly different between this Class I source and Class 0 sources, but the deuteration fraction of organic molecules is lower. A high CH_2DCN/CH_3CN ratio was later measured for SVS13A, suggesting that CH_3CN was formed via gas-phase reactions during the pre-stellar phase (Bianchi et al. 2022a).

In this work, we present NOrthern Extended Millimeter Array (NOEMA) CH_3CN, $CH_3{}^{13}CN$, DCN, and $C^{18}O$ observations toward SVS13A. Thanks to the wide bandwidth and high spectral resolution that are achievable with the PolyFiX correlator, along with the sensitivity achievable with NOEMA, we are able to study the temperature and kinematics of SVS13A through CH_3CN and DCN. In Sect. 2, we present the data and observations used in this paper. The results and analysis are detailed in Sect. 3. In Sect. 4, we discuss the scientific outputs and the conclusions are summarized in Sect. 5.

2. Observations

2.1. NOEMA observations

We observed SVS13A using the NOrthern Extended Millimeter Array (NOEMA) of the Institut de Radioastronomie Millimétrique (IRAM). The observations are part of the MPG – IRAM observing program PROtostars & DIsks: Global Evolution (PRODIGE; Project ID: L19MB002, PIs: P. Caselli and T. Henning). The observations consist of C-array configurations executed on December 29, 2019 and January 5, 2020, as well as D-array configurations executed on August 6, 2020 and September 7, 2020. In all executions, ten antennas were used. The on-source observing time is 2.74 h for the C-array and 2.22 h for the D-array. The bandpass calibrators were 3C84 and 3C454.3. Two phase calibrators, 0333+321 and 0322+222, were observed for all executions. The flux calibrators were LKHA101 and MWC349. Combining the C- and D-arrays with baselines 15.6–368 m (11.5–270.0 kλ) resulted in a synthesized beam size of 1.″2 × 0.″7 with natural weighting for line cubes and 1.″1 × 0.″6 with uniform weighting for the continuum image at ~220 GHz. The maximum recoverable scale is 22.″07.

The spectral setup consists of four broadband low-resolution windows and 39 narrow-band high-resolution windows within the broad-band frequency region. The broadband windows cover the frequency ranges of 214.7–218.8 GHz, 218.8–222.8 GHz, 230.2–234.2 GHz, and 234.2–238.3 GHz with a channel width of 2 MHz (~2.7 km s^{-1}). In this paper, we present three narrow-band windows that were designed to cover the CH_3CN J = 12–11 K-ladder, DCN J = 3–2, and $C^{18}O$ J = 2–1. The channel width of these three windows is 62.5 kHz (~0.08 km s^{-1}).

The data reduction was performed by the NOEMA pipeline calibration routine using the GILDAS-CLIC package[1], with additional manual flagging. We performed a phase-only self-calibration with the GILDAS `MAPPING` package using the continuum maps from the broad-band spectral windows (see Sect. 3.1). The iterative self-calibration was performed with solution intervals of 300 s, 135 s, and 45 s on the data which includes only line-free channels.

For the imaging of the line emission, the continuum subtraction for the narrow spectral windows is done using the `uv_baseline` task in the GILDAS/`MAPPING` package. Given the line-rich spectra, the line free regions are manually selected after

[1] https://www.iram.fr/IRAMFR/GILDAS

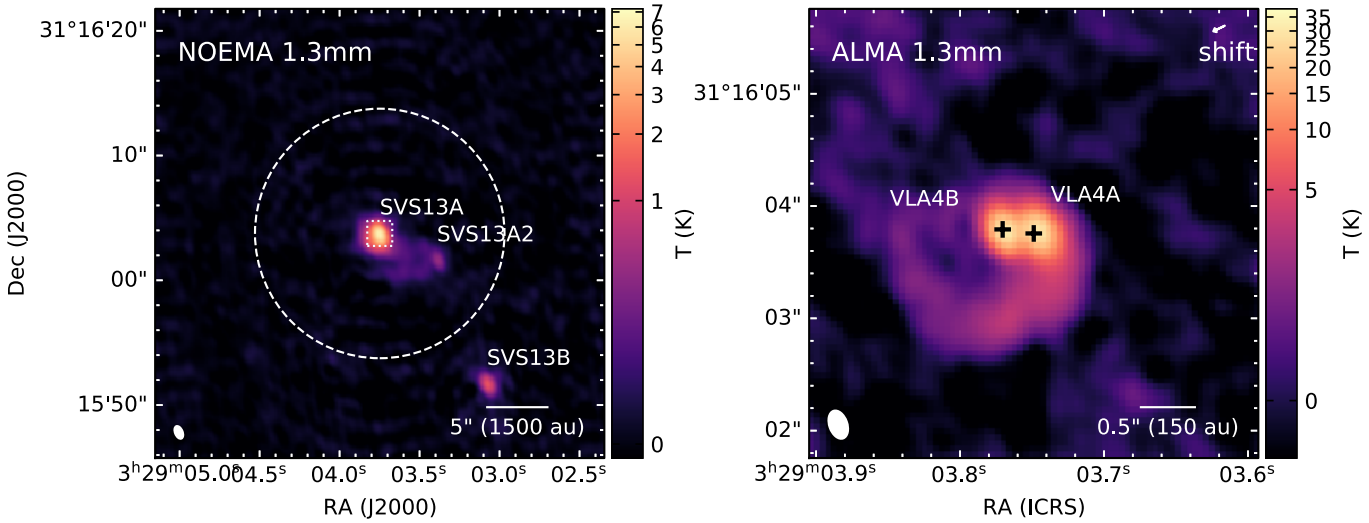

Fig. 1. 1.3 mm continuum emission toward the SVS13 region from NOEMA (*left*, rms ∼20 mK) and ALMA (*right*) observations. In the left panel, the dashed circle shows the primary beam of the NOEMA observation and the dashed box represents the FoV in the right panel. The black plus signs represent the positions of VLA4A/B from Hsieh et al. (2019). The arrow in the top right corner indicates the shift (0.″13) of the self-calibrated ALMA image.

visually examining the spectra. Imaging is done using the `clean` task with natural weighting for line cubes in order to increase the sensitivity. The continuum map was produced with robust = 1 Briggs weighting because the sensitivity is already high given the broadband width (4 GHz for each). With a manual clean mask, multi-scale clean algorithm is performed with a clean threshold of 1σ. The resulting data cubes have a beam size of 1.″23 × 0.″72 with a pixel size of 0.″15. The rms noise level is ∼0.013 Jy beam^{-1} for these image cubes with a channel width of ∼0.08 km s^{-1}. In comparison, the beam size of the continuum image is 1.″07 × 0.″61, with a pixel size of 0.″15, and the rms noise level is 0.5 mJy beam^{-1} (0.02 K).

2.2. ALMA archival data

We used the ALMA archival continuum and C^{18}O maps from VANDAM[2] (Tobin et al. 2016, 2018). The ALMA project ID is 2013.1.00031.S. The observations and data calibration are detailed in Tobin et al. (2018). The angular resolutions are 0.″26 × 0.″16 for continuum image and 0.″36 × 0.″26 for C^{18}O channel maps given the weighing and uv-range in use (see Tobin et al. 2018). The channel width of the C^{18}O maps is 0.25 km s^{-1}.

As the ALMA data from Tobin et al. (2018) were self-calibrated, we needed to apply a shift to the coordinates to match the position of VLA4A/B as observed in ALMA observations by Hsieh et al. (2019), for which no self-calibration was performed. The spatial resolutions of these observations are 0.″27 and 0.″11, respectively. The final shift applied to the ALMA observation is ∼0.″13 as shown in Fig. 1.

3. Results and analysis

3.1. Continuum images

The left panel of Fig. 1 shows the NOEMA continuum image. The multiple system consisting of SVS13A, SVS13A2, and SVS13B is resolved. Extended dust emission is also detected between SVS13A and SVS13A2, separated by ∼1600 au. The right panel shows a zoomed-in image on SVS13A from the high-resolution ALMA observation at 1.3 mm from VANDAM (Tobin et al. 2018). The close binary is resolved, as well as a spiral pattern that is interpreted as a fragmenting disk due to gravitational instability (Tobin et al. 2018).

3.2. CH_3CN and $CH_3{}^{13}CN$ emission

The high spectral-resolution narrowband spectrum of CH_3CN and $CH_3{}^{13}CN$ toward the peak continuum emission of SVS13A is shown in Fig. 2. The CH_3CN J = 12–11 K-ladder emission (K = 0 to K = 7) is clearly detected and, albeit with a lower signal-to-noise ratio (S/N), the $CH_3{}^{13}CN$ J = 12–11 K = 0 to K = 5 emission is also marginally detected (S/N∼3.1 for K = 5). A number of additional lines were identified using an automatic line identification algorithm (XCLASS, Möller et al. 2017), applied to the full broadband windows with a spectral coverage of 16 GHz. The LTE radiative transfer models for each identified molecule are provided. In order to check the line contamination, the identified lines with Einstein coefficients > 10^{-6} s^{-1} and E_{up} < 500 K are labeled. Based on the LTE model, the emission from the CH_3OCHO (A_{ul} = 6 × 10^{-6} and E_{up} = 382 K) and $^{33}SO_2$ (A_{ul} = 1 × 10^{-4} and E_{up} = 50 K), labeled in purple, is very weak or undetectable and should not significantly affect the later $CH_3{}^{13}CN$ analysis. However, a detailed study including full high-spectral resolution windows is required. We will present the full chemical inventory in a future paper (Hsieh et al., in prep.).

Figure 3 (left and center) shows the integrated intensity of the CH_3CN (12_3-11_3) and CH^{13}_3CN (12_1–11_1) emission, the brightest component with less contamination from other line emission. As the emission appears compact, we fit it with a Gaussian in *uv*-space. The derived size of the CH_3CN emission is 0.″42 ± 0.″02 × 0.″34 ± 0.″01 (∼110 au), likely overestimated due to insufficient resolution. The size of $CH_3{}^{13}CN$ is found to be 0.3″ × 10^{-5}″ from the fitting for which the minor axis of 10^{-5} arcsec is unlikely to be constrained. Indeed, higher-resolution observations (beam ∼0.″5) derived a smaller size of

[2] https://dataverse.harvard.edu/dataverse/VANDAM

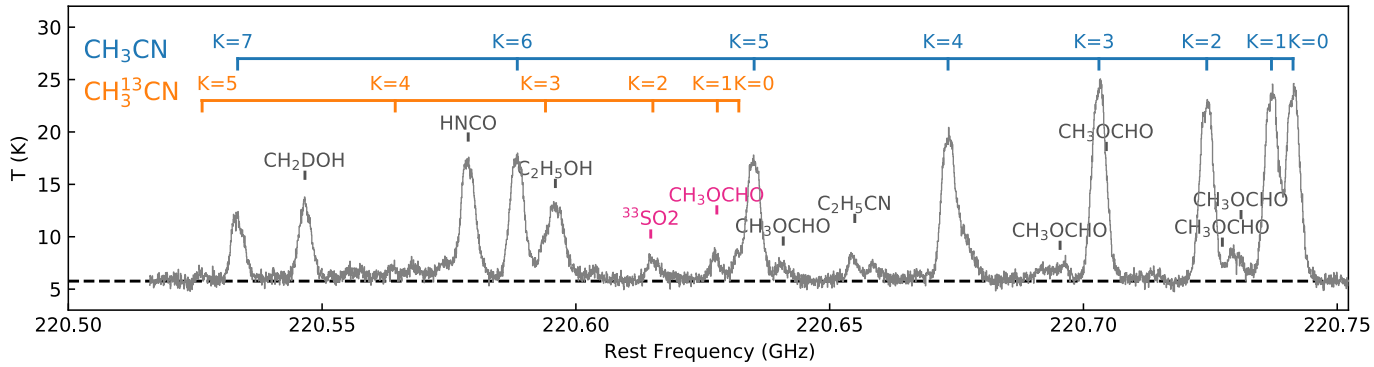

Fig. 2. Spectrum of CH_3CN and $CH_3{}^{13}CN$ toward the peak of the continuum emission. The labels of the line frequencies, blue (CH_3CN), orange ($CH_3{}^{13}CN$), grey and pink bars, are shifted assuming a systemic velocity of 8.1 km s^{-1}. We only marked lines with an Einstein coefficient > 10^{-6} s^{-1} and E_{up} < 500 K; the Einstein coefficients are 6×10^{-6} s^{-1} (E_{up} = 382 K) for the CH_3OCHO line and 1×10^{-4} s^{-1} (E_{up} = 50 K) for the $^{33}SO_2$ line in pink while both are very weak or undetectable based on the XCLASS model from wideband spectra including more transitions. The horizontal dashed line indicates the continuum level of 5.8 K determined from line free channels. The sensitivity per channel is 380 mK.

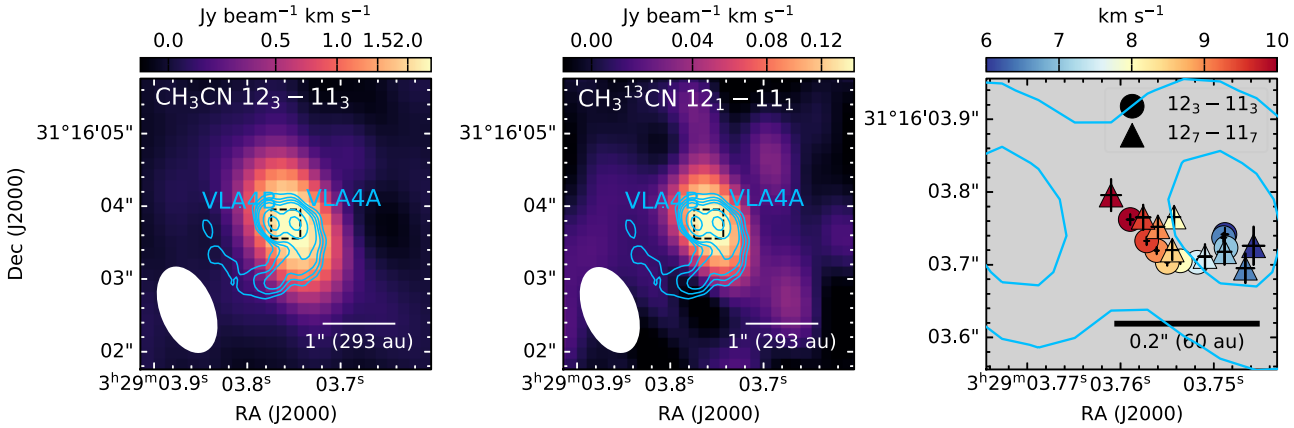

Fig. 3. Integrated intensity map of CH_3CN 12_3–11_3 emission (4.0–12.0 km s^{-1}) shown to the left. The contours represent the ALMA 1.3 mm continuum emission from Fig. 1. with levels of 3σ, 5σ, 7σ, 10σ, 30σ, and 70σ. The dashed box shows the field of view in the right panel. The central panel shows the same details as the left, but for $CH_3{}^{13}CN$ 12_1–11_1 emission. Gaussian centers from the *uv*-domain fitting shown on the right. The colored circles (CH_3CN 12_3–11_3) and triangles (CH_3CN 12_7–11_7) show the positions from the *uv*-domain fitting, with the color indicating the velocity.

0.″3 (90 au) for the COM emitting region (Belloche et al. 2020), which is likely also an upper limit (see Sect. 3.3).

3.3. CASSIS fitting

The CH_3CN K-ladder gives us the opportunity to study the physical conditions of the hot gas. We performed the CASSIS[3] (Vastel et al. 2015) Markov chain Monte Carlo (MCMC) fitting to the CH_3CN (J = 12–11, K = 0–7) and $CH_3{}^{13}CN$ (J = 12–11, K = 0–5) emission. The line parameters are taken from CDMS[4] (Müller et al. 2005; Endres et al. 2016), while the parameters for CH_3CN and $CH_3{}^{13}CN$ were originally provided by Müller et al. (2015) and Müller et al. (2009), and references therein. The partition function $Q(T)$ of CH_3CN includes vibrational contribution up to v8 = 1, while only the ground state is available for $CH_3{}^{13}CN$ in the CDMS database. Vibrational correction of the isotopologue $CH_3{}^{13}CN$ can be done by scaling $Q(T)$, using the ratios of the $Q(T)$ of CH_3CN with and without a vibrational contribution. Since the ground state $Q(T)$ of CH_3CN and that of $CH_3{}^{13}CN$ are almost the same (difference <0.06% at T < 500 K), the scaled partition function of $CH_3{}^{13}CN$, namely, vibrational-corrected, will be the same as that of the CH_3CN one within a factor of 0.06 %. We thus use the partition function of CH_3CN including vibrational contributions for the $CH_3{}^{13}CN$ in our MCMC fitting. We excluded the CH_3CN K = 4 component, $CH_3{}^{13}CN$ K = 3 component, and the blueshifted wing of the CH_3CN K = 6 component from our fitting due to contamination from nearby lines (see Fig. 2). A continuum level of 5.77 K was determined based on the line free channels (Fig. 2) and taken as an input for the simultaneous line fit performed by CASSIS. Technical information on the MCMC sampling is detailed in Appendix A.

Figure 4 (top panel) shows the best-fit spectrum with a one-component LTE model. Table 1 lists the best-fit column density, rotation temperature, linewidth, source size and central velocity, and isotopologue ratio (CH_3CN/$CH_3{}^{13}CN$). The posterior probability distribution of each parameter is shown in Fig. A.7. The resulting CH_3CN column density and temperature are 5.13×10^{16} cm^{-2} and 247.8 K, respectively, with a source size of 0.″27. The column density and temperature are larger by a factor of 1.3–8.5 and 1.4–1.7 than that in Belloche et al. (2020) and Yang et al. (2021) (Table 1). The difference between our LTE model and the literature most likely comes from the

[3] http://cassis.irap.omp.eu/
[4] https://cdms.astro.uni-koeln.de/cdms/portal/

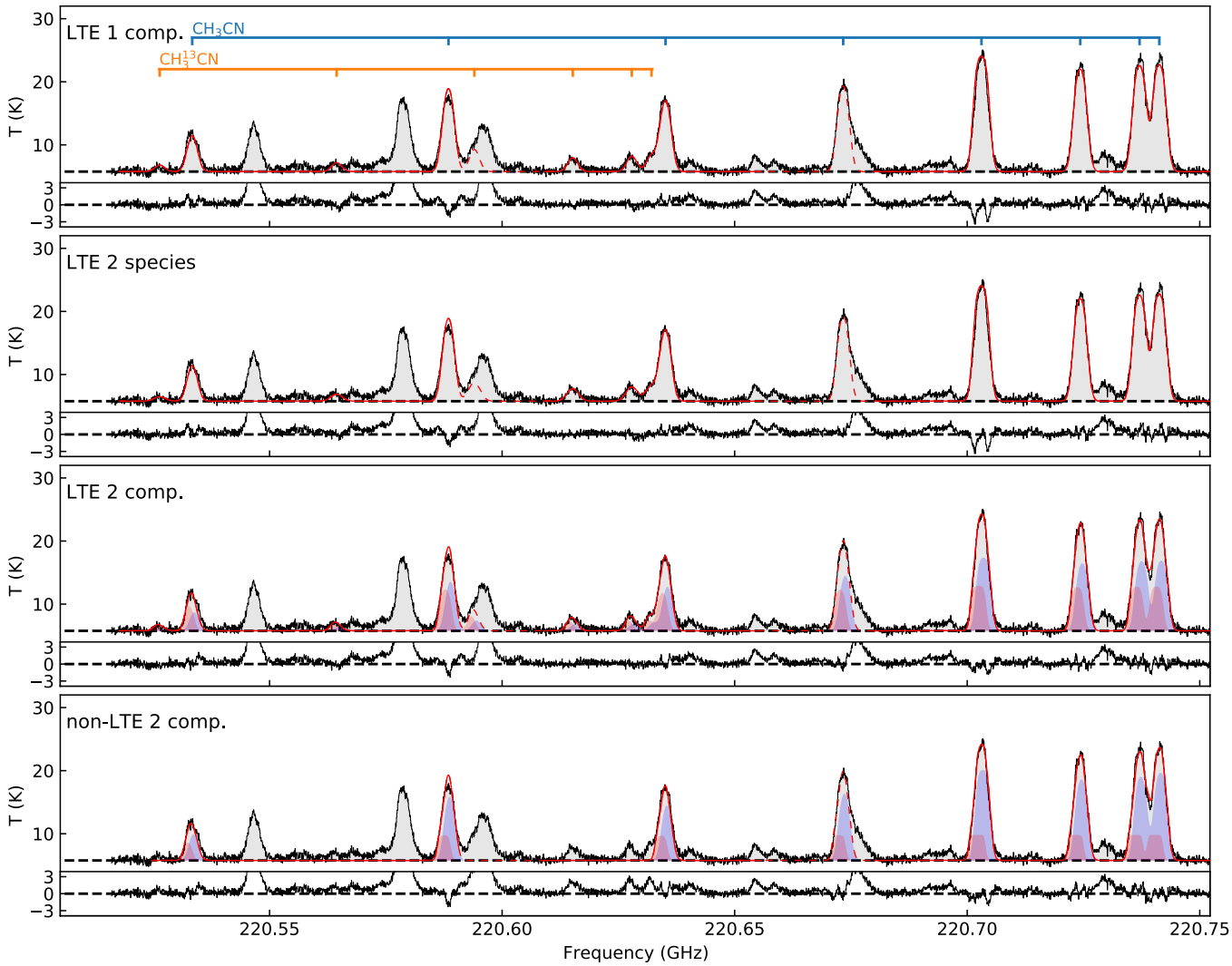

Fig. 4. Modeled CH_3CN and $CH_3{}^{13}CN$ spectra overlaid on the observed spectra. The first panel shows the LTE model one velocity component fitting. The second panel is the same as the first panel but treats CH_3CN and $CH_3{}^{13}CN$ as two species with independent temperature, velocity and linewidth. The third panel is the LTE two velocity component fitting, while the fourth panel shows the non-LTE one. The red curve shows the modeled spectrum. The K = 4 component of CH_3CN and K = 3 component of $CH_3{}^{13}CN$ suffer from severe line contamination so they were not included in the fitting. The model in these frequency ranges is shown with the dashed line. The red and blue shaded areas in the two bottom panels represent the modeled spectrum from the individual components. The residual from the best-fit is shown in the bottom frame of each panel. The best-fit parameters are listed in Table 1 and the corner plots are shown in Appendix A.

assumption of the source size in the previous works. In Belloche et al. (2020), a source size of 0.″3 based on Gaussian fitting in uv-space was adopted, while Yang et al. (2021) fixed a size of 0.″5 for the unresolved case. As shown in Fig. A.7, the column density and excitation temperature are highly correlated with the source size; we note here that the optical depths from the fitting are 0.36–3.20 for the CH_3CN J = 12–11, K = 0–7 emission. It is clear that the adopted source size will determine the column density and excitation temperature as well as the optical depth τ, although this may not significantly change the relative abundances of COMs in the literature (Belloche et al. 2020; Yang et al. 2021). In our case, with the source size as a free parameter, the optical depth is determined based on the line intensity ratios. Because the $K = 3n$ (i.e., 3 and 6) transitions have a degeneracy larger than the others by a factor of 2, increasing the column density will change their optical depths much more than the others (i.e., the $K = 3n$ components will saturate faster than their neighboring transitions). The opacities of the best-fit model are listed in Table A.2. In this case, the source size scales the intensities of all transitions, and the temperature affects the level populations as well as the optical depths. As a result, the high sensitivity data enable us to determine the optical depths as well as column density from the accurate measurement of the intensity ratios.

This one-component model does not adequately reproduce the peak of the optically thick transitions (K = 0–3). In particular, for the K = 3 component, the synthetic line profile is much broader than that of the observation (see also Fig. A.3). This suggests that the optical depths are not properly estimated. Interestingly, the isotopologue ratio $[CH_3CN/CH_3{}^{13}CN] \simeq 16$ is surprisingly low compared to the canonical ratio $^{12}C/^{13}C \simeq 68$ (Milam et al. 2005). A possibility is that the optical depth, τ, is not properly estimated by this simple one-component model. We therefore performed a fitting that takes CH_3CN and $CH_3{}^{13}CN$ as independent species with different temperatures, velocities, and linewidths (Fig. 4, second panel). This gives us very different

Table 1. CH_3CN fitting results.

Model	Component	N_{CH_3CN} (10^{16} cm^{-2})	T_{rot} (K)	FWHM (km s^{-1})	Size (arcsec)	log(n_{H2}) (cm^{-3})	V_{LSR} (km s^{-1})	$\frac{CH_3CN}{CH_3{}^{13}CN}$
LTE model	–	$5.13^{+0.07}_{-0.06}$	$247.8^{+1.4}_{-1.4}$	$3.34^{+0.01}_{-0.01}$	$0.273^{+0.001}_{-0.001}$	–	$8.099^{+0.003}_{-0.003}$	$15.6^{+0.2}_{-0.2}$
LTE two species	CH_3CN	$5.05^{+0.07}_{-0.07}$	$246.6^{+1.4}_{-1.4}$	$3.33^{+0.01}_{-0.01}$	$0.274^{+0.001}_{-0.001}$	–	$8.094^{+0.003}_{-0.003}$	$25.2^{(a)}$
	$CH_3{}^{13}CN$	$0.20^{+0.02}_{-0.01}$	$166.8^{+10.5}_{-10.9}$	$3.91^{+0.06}_{-0.06}$	0.27^{*}	–	$8.117^{+0.032}_{-0.032}$	–
LTE 2-comp	Extend	$2.77^{+0.08}_{-0.08}$	$189.2^{+2.9}_{-2.9}$	$3.02^{+0.02}_{-0.01}$	$0.247^{+0.002}_{-0.003}$	–	$7.490^{+0.023}_{-0.024}$	$24.6^{+1.0}_{-0.9}$
	Compact	$11.0^{+0.9}_{-0.8}$	$275.8^{+7.7}_{-8.0}$	$2.67^{+0.02}_{-0.02}$	$0.154^{+0.004}_{-0.003}$	–	$8.950^{+0.023}_{-0.024}$	$16.84^{+0.6}_{-0.6}$
Non-LTE 2-comp	Extend	$1.74^{+0.05}_{-0.04}$	$211.9^{+2.9}_{-2.9}$	$3.00^{+0.01}_{-0.01}$	$0.287^{+0.002}_{-0.003}$	$6.79^{+0.04}_{-0.03}$	$7.739^{+0.014}_{-0.015}$	–
	Compact	$7.18^{+0.44}_{-0.40}$	$193.6^{+13.6}_{-10.9}$	$2.38^{+0.04}_{-0.04}$	$0.141^{+0.004}_{-0.004}$	$>8.07^{+0.40\,(b)}_{-0.43}$	$9.321^{+0.024}_{-0.027}$	–
Belloche et al. (2020)	–	4	180	$4.0^{(*)}$	$0.3^{(*)}$	–	–	–
Yang et al. (2021)	–	$0.6^{+0.18}_{-0.13}$	$150^{(c)}$	–	$0.5^{(*)}$	–	–	–

Notes. $^{(*)}$The parameter is fixed. $^{(a)}$The value is derived from the $CH_3CN/CH_3{}^{13}CN$ column density ratio. $^{(b)}$The value is considered as a LTE case, because the posterior distribution reaches the upper boundary of 5×10^8 cm^{-3} in the MCMC modeling given a critical density of $\sim 10^8$ cm^{-3} for CH_3CN J = 12–11, K = 0–7. $^{(c)}$The fitting was done with a step of 50 K.

temperatures for CH_3CN (246.6 K) and $CH_3{}^{13}CN$ (166.8 K), implying that they originate from different regions. In addition, the observed line profile shows an asymmetric structure; the emission is stronger in the blueshifted side in the low-energy transitions, but reversed in the K = 7 component (Fig. A.3).

It is most likely that a one-component model cannot adequately fit the CH_3CN emission from this known complex structure. We thus performed a two-component LTE model to fit the observational spectrum, which results in a better fit (Fig. 4, third panel); the synthetic spectral profile and observed profile have similar emission peaks in the K = 0 and K = 1 components and similar widths in the K = 3 component. The best-fit parameters are listed in Table 1 and their opacities are listed in Table A.2. These two components are assumed to be spatially separated, that is, the interaction mode is turned off in our CASSIS setup. Resolving such a complicated scenario requires data with a higher spatial resolution. In fact, the binary system has been spatially resolved by continuum emission (Tobin et al. 2018) and velocity gradient toward SVS13A is revealed via other COM emission (Diaz-Rodriguez et al. 2022). A compact, optically thick, redshifted component and a thin blueshifted component are separated, which is in agreement with the asymmetric structures in the line profiles. This result suggests that the traditional rotation diagram or one-component model cannot accurately describe this complex profile. In this case, the two-component model implies the presence of an optically thick component. This would result in an underestimation of the column density when using one-component fitting. It is, however, noteworthy to observe that although the isotopologue ratio is higher in the two-component model as compared to the one-component model, they are still lower than the canonical ratio (see Table 1).

Furthermore, we estimated the H_2 density by applying the non-LTE radiative transfer code RADEX (van der Tak et al. 2007) in CASSIS (Fig. 4, bottom panel). The collision rates are taken from LAMDA[5] as calculated by Green (1986). We note here the geometry of the emitting gas is described as a sphere in the RADEX calculation and the two components are spatially separated. We have a compact optically thick component and a relatively extended optically thin component at the blue- and redshifted sides, similarly to the LTE case (Table 1). The compact component is close to LTE with $n_{H_2} \sim 1.2 \times 10^8$ cm^{-3} (critical density $\sim 10^7$–10^8 cm^{-3} for a temperature of $\sim$200 K). Given the n_{H_2} densities of 6.2×10^6 cm^{-3} and $>1.2 \times 10^8$ cm^{-3}, we estimated the enclosed masses of 1.1×10^{-5} $M_\odot$ within 0.″287 (r = 42 au) for the extended component and $>2.4 \times 10^{-5}$ $M_\odot$ within 0.″141 (r = 21 au) for the compact component. These values are smaller than the disk masses (0.004–0.009 $M_\odot$ for VLA4A and 0.009–0.030 $M_\odot$ for VLA4B) derived from the dust continuum emission (Diaz-Rodriguez et al. 2022). One possibility is that the optically thick CH_3CN emission does not trace the dense disk midplanes. Alternatively, the n_{H_2} density can be higher than the critical density by about two orders of magnitude. We note that here the comparison simply assumes a uniform density to give a very rough idea.

3.4. Kinematics of CH_3CN

For a spectrally resolved, optically thin line, the peak position of the line emission is believed to represent the most likely location of the emitting gas (Sargent & Beckwith 1987; Harsono et al. 2013). To disentangle the velocity structure of the CH_3CN, we performed a *uv*-domain Gaussian fitting to the spatial emission at different velocity channels. For CH_3CN, the thermal width of CH_3CN (12–11) at 200 K is $\sim$0.5 km s^{-1}. Thus, we took a step of 0.5 km s^{-1} to increase S/N, while resolving the gas kinematics, along with a velocity range from 6 to 10 km s^{-1} (Fig. A.3). We used the K = 3 and K = 7 components, which do not suffer as much from contamination of other lines (Fig. 2). The K = 7 emission is most likely optically thin, and the K = 3 emission (although it is optically thick) has the highest S/N among the K-ladder transitions. Figure 3 (right) shows the fitted central positions from different velocities. The emitting centers show similar trends in these two transitions; the majority of

[5] https://home.strw.leidenuniv.nl/~moldata/

the CH_3CN emission is associated with VLA4A, which is considered to be the warmer source with a higher accretion rate (Hsieh et al. 2019). A clear velocity gradient from the west to the east is seen. The direction of this velocity gradient is broadly consistent with the position angle of the circumstellar disk around VLA4A and the circumbinary disk (Diaz-Rodriguez et al. 2022); in the literature, ethylene glycol (aGg'-$(CH_2OH)_2$) is found to trace rotating gas from the circumstellar disk of VLA4A (Diaz-Rodriguez et al. 2022). By comparing these emitting centers to kinematic models, we find that the CH_3CN emission is most likely associated with a disk or a rotating envelope around VLA4A, rather than that of VLA4B or the circumbinary disk (see Appendix B). However, this analysis shows that the velocity gradient from CH_3CN cannot be interpreted by a simple rotationally supported disk or from angular momentum conservation. It is then likely that CH_3CN and aGg'-$(CH_2OH)_2$ trace different gas components. High angular-resolution observations are required to confirm the origins of the CH_3CN emission.

3.5. A streamer in the DCN and $C^{18}O$ emission

Figure 5 shows the NOEMA DCN (3–2) integrated intensity map. The DCN emission traces the central binary system and reveals a streamer in the east. Interestingly, this streamer matches the tail of the spiral structure that is seen in the continuum emission and extends this spiral to outer regions at a few arcsec (~2.″4, 700 au). These kinds of streamers connecting inner and outer regions have been recently identified in embedded systems and are considered to be infalling flows that provide the material supplying the growth of disks and central protostars (Pineda et al. 2020; Alves et al. 2020; Murillo et al. 2022; Cabedo et al. 2021; Thieme et al. 2022; Valdivia-Mena et al. 2022).

Because the DCN spectral profile is likely to have originated from a complex structure (Fig. 6), we employed a multiple-component fitting in order to isolate the streamer and further study its kinematics. We fit the hyperfine structure of the DCN (3–2) line emission using PySpecKit (Ginsburg & Mirocha 2011) with the line parameters from CDMS (Müller et al. 2005; Endres et al. 2016), for which the DCN parameters were taken from Brünken et al. (2004) and references therein. Although the satellite line emission is marginally detected (Fig. 6), the weak emission in the streamer suggests that the DCN (3–2) emission is optically thin. Toward the center, the hyperfine structure is not clearly seen with the complex and broad line emission. However, analyzing this DCN structure toward the center is beyond the scope of this paper. Thus, we assumed a total optical depth of 0.1 in the hyperfine structure fitting (HFS). Toward the center region, several velocity components are revealed from the spectra. We therefore performed a hyperfine fitting with multiple velocity components (up to three, see Appendix D). We only focus on the regions where the peak intensity has a S/N>25 from the spectrum to distinguish the streamer from the more extended emission background. Figure 6 shows the maps of the fitted centroid velocity and linewidth of the blueshifted component which traces the streamer. A small velocity gradient ~0.12 km s^{-1} arcsec^{-1} along the streamer with a relatively narrow line width of ~0.7 km s^{-1} is revealed. We note that a very small velocity break from 8.4 km s^{-1} to 8.1 km s^{-1} comes from a change of fitting from two to three velocity components (see Appendix D).

Using ALMA, Tobin et al. (2018) found that the dusty spiral from the continuum emission aptly matches the $C^{18}O$ (2–1) blueshifted emission (6.0–8.5 km s^{-1}, their Fig. 15). Figure 7 shows the NOEMA $C^{18}O$ (2–1) channel maps at 7.7–8.5 km s^{-1} in comparison with the streamer traced by the DCN and continuum emission. Although at the velocity of the DCN streamer (~8.3–8.6 km s^{-1}, Fig. 6), the $C^{18}O$ emission is offset from the DCN emission, the emission peak matches the inner spiral at a velocity ≲8.2 km s^{-1} well; and this velocity well connects the DCN blueshifted end from ~8.3 km s^{-1} to a velocity of ~7.7 km s^{-1} in the inner region (see also Fig. C.2 from the ALMA data). The channel maps of DCN/$C^{18}O$ in the region of interest are provided in Appendix C.

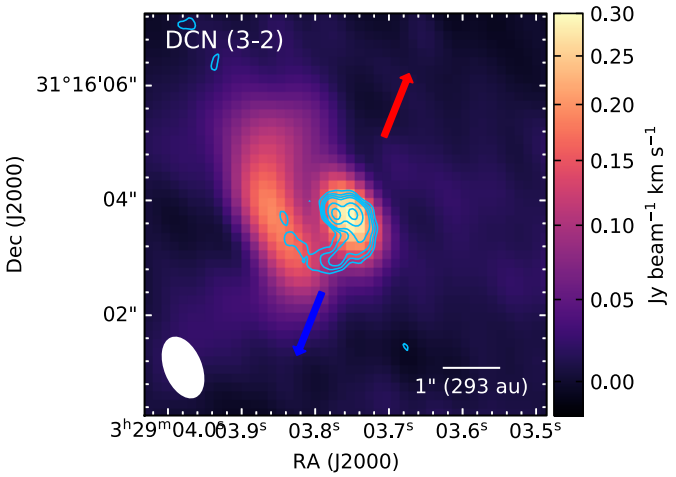

Fig. 5. Integrated intensity map of DCN (3–2) over a velocity range of 8.26–8.8 km s^{-1}. The contours represent the ALMA 1.3 mm continuum emission with levels at 3, 5. 7, 10, 30, and 70σ. The blue and red arrows indicate the CO outflow directions from Lefèvre et al. (2017).

Figure 6 also shows the DCN and $C^{18}O$ line profiles at four selected positions from the streamer. In the outer part of the streamer (i.e., position 4), the $C^{18}O$ emission is offset from the DCN emission in velocity. In the middle part of the streamer (i.e., position 3), the DCN and $C^{18}O$ lines have a similar centroid velocity. At position 2, while the DCN emission becomes relatively weak compared with that of $C^{18}O$, the lines show similar profiles. It seems that along the streamer, the physical properties change, producing a different DCN/$C^{18}O$ integrated intensity ratio. However, the velocity gradient revealed by DCN emission is broadly consistent with that of $C^{18}O$ at velocities ≲8.3 km s^{-1} (Fig. C.2) and might trace an infall of material. More observations at higher spatial resolutions are needed to test for infall via modeling.

To estimate the mass of the streamer, we calculated the DCN column density (Fig. 8) over a velocity range of 7–10 km s^{-1} targeting the streamer. The column density is calculated under assumptions of LTE and optically thin emission (i.e., Eq. (80) in Mangum & Shirley 2015). Due to the lack of measurements for the DCN collision rates, we consider those for HCN (van der Tak et al. 2020). The critical density of HCN (3–2) is 1.0×10^7 cm^{-3} at 20 K and 5.7×10^6 cm^{-3} at 50 K in the optically thin limit (Shirley 2015). This is close to the lower bound estimated from previous works $n_{H_2} \geq 10^6$ cm^{-3} within 600 au using H_2CO (Bianchi et al. 2017). Thus, the LTE assumption might cause an underestimate of the actual streamer mass. The excitation temperature is estimated considering the luminosity of SVS13A (45.3 $L_\odot$) and the projected distance to VLA4A (i.e., $T_d = \frac{2.4\times10}{(r/pc)^{2/5}}(\frac{L}{10^6 L_\odot})^{1/5}$, Goldreich & Kwan 1974). This gives a temperature of ~35–45 K in the streamer. To exclude the extended DCN emission, we employ a mask with a peak

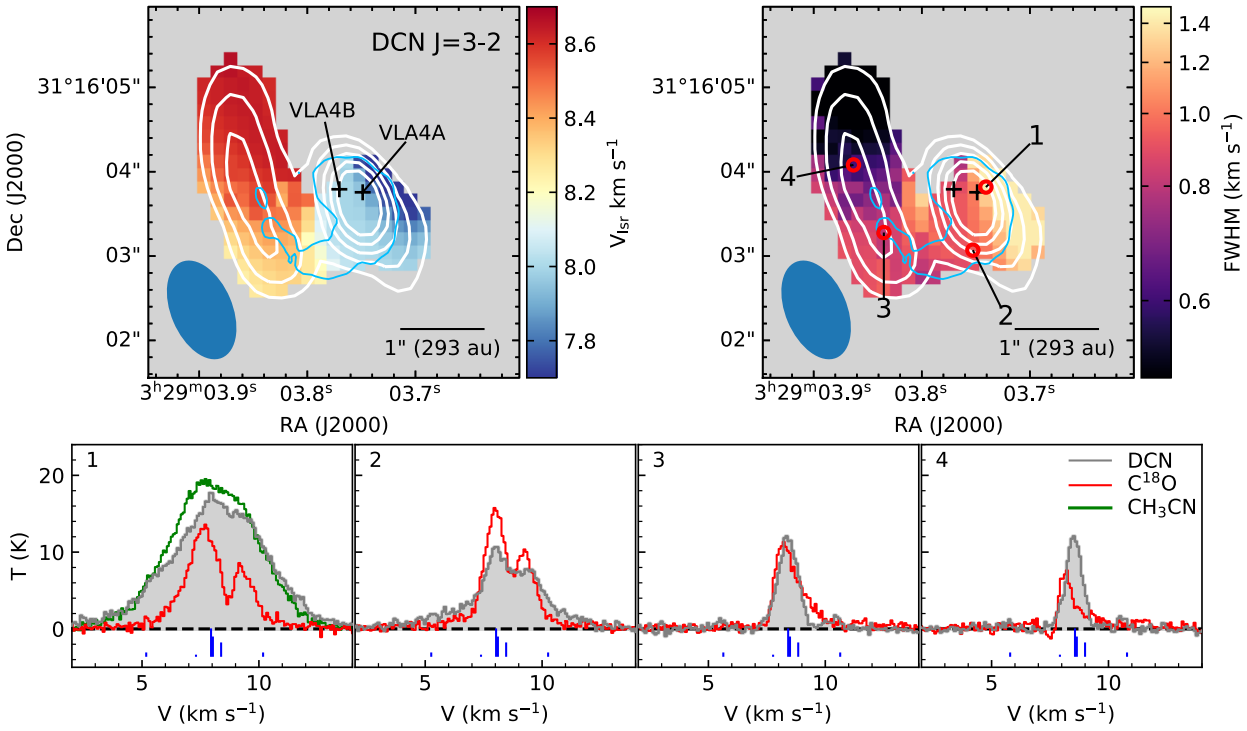

Fig. 6. DCN (3–2) centroid-velocity (*top-left*) and linewidth (*top-right*) maps from the blueshifted component in the hyperfine structure fitting (see Appendix D). The white contours show its peak intensity. The contour levels start at 25σ and increase in 5σ step, where σ = 0.3 K. The blue contour shows the ALMA 1.3 mm continuum emission at the 3σ level. Spectra of DCN (3–2), C^{18}O (2–1), and CH$_3$CN (12$_3$–11$_3$) toward the four positions marked in the right panel (*bottom*). The blue bars show the relative intensities of the DCN (3–2) hyperfine structure at the velocity of the blueshifted component (see Appendix D).

emission above 25 σ and a linewidth <1 km s^{-1} from the hyperfine fitting (Fig. 6). This gives a conservative lower limit to the streamer area. Figure 8 shows the DCN column density of the streamer. Adopting the same LTE excitation state for C^{18}O, we further estimate the abundance ratio of [DCN]/[C^{18}O] to be $\sim 1.36 \times 10^{-3}$ at position 3 in Fig. 6. We note that with a different T_{ex} = 20–80 K, this abundance ratio varies from (1.54–1.28) $\times 10^{-3}$. Taking the canonical ISM value of CO/C^{18}O~560 and CO abundance of 10^{-4} (Wilson & Rood 1994), we find a DCN abundance of $\sim 2.4 \times 10^{-10}$, with respect to H_2. As a result, the streamer mass is estimated to be $\gtrsim 0.0042\ M_\odot$.

4. Discussion

4.1. Physical and chemical conditions from CH_3CN

Table 1 lists the physical conditions of SVS13A derived from the CH$_3$CN K-ladder, with different models. Besides the main CH$_3$CN isotopologue, the high-sensitivity data also allowed us to detect the isotopologue CH$_3$ ^{13}CN (Fig. 2). With the LTE one-component model, the abundance ratio CH$_3$CN/CH$_3$ ^{13}CN is found to be ~20. This is surprisingly low given the interstellar isotopologue ratio [^{12}C]/[^{13}C]~68 (Milam et al. 2005). In IRAS16293, Calcutt et al. (2018) find the column density ratios CH$_3$CN/CH$_3$ ^{13}CN~67 and CH$_3$CN/^{13}CH$_3$CN~77. ^{12}C/^{13}C ratio can be affected by selective photodissociation and fractionation. For example, the ^{12}CO/^{13}CO ratio is found to vary by a factor of >4 from the inner to outer parts of the TW Hya disk (Yoshida et al. 2022). As selective photodissociation is suggested to affect the isotopologue ratios in the disk atmosphere (Miotello et al. 2014; Smirnov-Pinchukov et al. 2020), this mechanism can decrease ^{12}C/^{13}C ratio by destruction of the main isotopologue. On the other hand, isotopic fractionation reaction can enhance the ^{13}C abundances in molecules but usually happen in cold region with exothermic reactions (Roueff et al. 2015). It is noteworthy that in SVS13A, CH$_3$CN is suggested to be synthesised via gas-phase reactions during cold prestellar phase (Bianchi et al. 2022a). Alternatively, the CH$_3$CN column density is underestimated due to an inaccurate opacity correction. This scenario is similar to that reported by Diaz-Rodriguez et al. (2022) with the ^{13}CH$_3$OH/CH$_3$ ^{18}OH~3, significantly smaller than the expected value of ~7. Broadly speaking, the optically thick CH$_3$CN emission (which depends on K-transition) and the optically thin CH$_3$ ^{13}CN emission can trace a different region or layer.

Thus, we conducted a fitting procedure assuming that CH$_3$CN and CH$_3$ ^{13}CN are independent species (i.e., different V_{lsr}, ΔV, T_{ex} and N_{mol}, Table 1 LTE two species). However, the source size of CH$_3$ ^{13}CN was fixed to 0.″27 to match that of CH$_3$CN. Given that the emission of CH$_3$ ^{13}CN is optically thin, the derived column density is inversely proportional to the square of the source size. As a result, the temperature of CH$_3$ ^{13}CN is significantly lower than that of CH$_3$CN. This result (Table 1) implies that the CH$_3$ ^{13}CN with a smaller optical depth traces a region different from CH$_3$CN, which might explain the small column density ratio.

We also employed a two velocity-component model, in an attempt to resolve the issues of optical depth (K = 0–3) and asymmetric line profile (Fig. A.3). A relatively optically thin blueshifted component (τ = 0.28–3.2) and an optically thick (τ = 0.8–6.4) redshifted component are found (Fig. 4). The residual from the optically thick K = 3 component is now

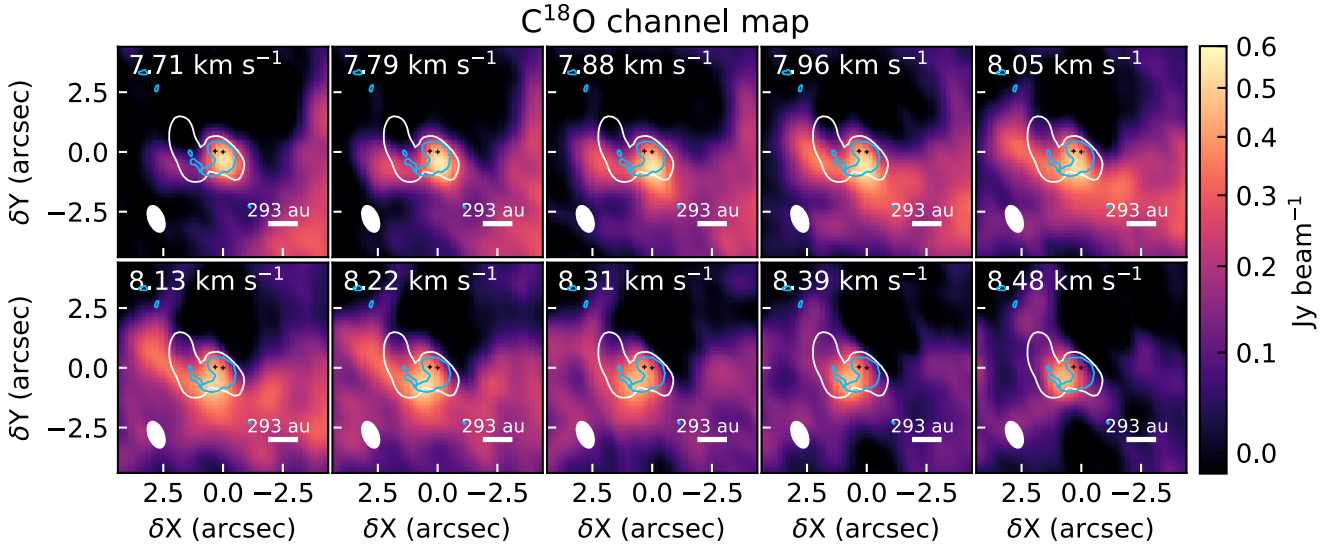

Fig. 7. $C^{18}O$ (2–1) channel map with the velocity range from 7.7–8.5 km s^{-1}. The blue contour shows the ALMA continuum emission at 3σ and the white contour shows the DCN (3–2) peak intensity map at 25σ

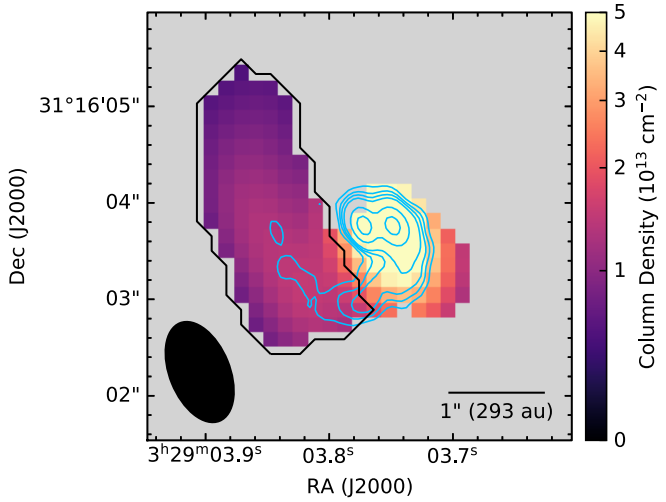

Fig. 8. DCN column density map. The blue contours represent the ALMA 1.3 mm dust continuum emission. The black polygon encloses the area that is used to measure the mass of the streamer.

significantly decreased. Table 1 lists the fitted parameters from the MCMC fitting as shown in Fig. 4. The result implies that an optically thick compact component was missed in the one-component model, while the optically thin component can dominate the line emission. Because of the missing of the optically thick component due to insufficient spatial resolution, the column density of the CH_3CN can be severely underestimated. It is noteworthy that, with the two-velocity component model, the isotopologue ratios of $\frac{CH_3CN}{CH_3{}^{13}CN}$ (~25 and ~17) are still too low compared to the canonical value (~68; Milam et al. 2005). Therefore, the fitting procedure taking $CH_3{}^{13}CN$ as an independent species is still required.

Previous works conducted non-LTE analysis using different chemical tracers to estimate the H_2 density (n_{H_2}) toward SVS13A. Using the IRAM 30 m telescope, Codella et al. (2016) estimate a H_2 volume density of $\geq 3 \times 10^7$ cm^{-3} inside a small radius of 25 au with a temperature of 150–260 K through HDO observations. This compact source is believed to originate from a hot corino. With CH_3OH, Bianchi et al. (2017) found a similarly compact component with $n_{H_2} > 10^8$ cm^{-3} but lower $T_{kin} \sim 80$ K, within a radius of ~35 au, and an additional extended component with $n_{H_2} > 10^6$ cm^{-3} and $T_{kin} < 70$ K within ~350 au. Recently, Codella et al. (2021) suggest that the SO, SO_2, and H_2CS emission from SVS-13A is confined within the hot corino, with a size 60–120 au, $n_{H_2} \geq 1 \times 10^5$–$6 \times 10^6$ cm^{-3} and $T_{kin} = 100$–300 K. In our non-LTE two-component models of CH_3CN, we find a compact component with a size of 0.″14 (40 au), with $n_{H_2} > 10^8$ cm^{-3} (LTE) and an extended component with a size of 0.″29 (85 au) and $n_{H_2} \sim 6 \times 10^6$ cm^{-3}. Our result is broadly consistent with the literature; most likely, SVS13A consists of a compact high-density hot corino with a diameter of 50–70 au, and an extended warm structure up to ~120 au. It is noteworthy that with the high-resolution ALMA observation, Diaz-Rodriguez et al. (2022) decompose SVS13A into three disks: VLA4A (67 × 62 au), VLA4B (unclear from line observation), and a circumbinary disk (240 × 180 au).

Codella et al. (2016) reported the HDO observation toward SVS13A; the non-LTE analysis gives the best-fit column density of 4×10^{17} cm^{-2}, and a temperature of 200 K with a source size of 0.″2. The source size as well as the linewidth of ~4.5 km s^{-1} (H_2O, Kristensen et al. 2012) are broadly consistent with that of CH_3CN. Further, Codella et al. (2016) found an upper limit of water column density $\leq 8 \times 10^{17}$ cm^{-2} based on a $H_2{}^{18}O$ non-detection. If we assume that the CH_3CN compact component originates from the same region as the HDO and water, we obtain lower limits of CH_3CN abundance relative to H_2O ≥18–26% for the compact component (Table 1). This is higher than the values reported in comets (Hyakutake: 0.01%; Hale-Bopp: 0.02%; 2001 A2: 0.028%; 73P/SW3: 0.030%; 67P: 0.59%) and between interstellar sources (IRAS 16253: 0.25%; Sgr B2(N): 30%) (Mumma & Charnley 2011; Bockelée-Morvan & Biver 2017; Rubin et al. 2019).

4.2. Accretion flow traced by DCN?

During the embedded phase of a protostar, infall of material plays a crucial role in supplying material to the central source and protoplanetary disk. Recent studies have detected large

infalling streamers at an early stage, which are believed to affect the protostellar accretion (Pineda et al. 2020; Alves et al. 2020; Cabedo et al. 2021; Ginski et al. 2021; Murillo et al. 2022; Garufi et al. 2022; Thieme et al. 2022; Valdivia-Mena et al. 2022).

In SVS13A, the streamer is seen in DCN, $C^{18}O$ and partially in dust continuum emission (see Sect. 3.5), connecting the outer envelope with the central binary. At early evolutionary stages, large infalling streamers (1000 s of au) are identified via Carbon-chain species such as HC_3N toward Per-emb-2 (Pineda et al. 2020) and HC_5N toward IRAS 16293-2422 (Murillo et al. 2022); these molecules usually trace less chemically evolved regions, while the deuterated species DCN traces relatively chemically evolved materials. The fresh materials, together with the enormous streamers, in the literature suggest that these streamers originate from outside the cloud core. In contrast, the streamer toward SVS13A via DCN is much smaller, that is, ~700 au. It is unclear if this streamer is extended farther away or not due to the insufficient sensitivity or lack of proper tracers.

The velocity gradient along the streamer revealed by DCN and $C^{18}O$ suggests it is related to infalling material towards the protostars. The total mass of this streamer is estimated to be $M_{\rm streamer} \sim 0.0042 M_\odot$ (Sect. 3.5 and Fig. 8). Assuming a free-fall collapse, the mass infalling rate from the streamer can be estimated following Pineda et al. (2020):

$$\dot{M}_{\rm infall} = \frac{M_{\rm streamer}}{t_{\rm ff}}, \quad (1)$$

where $t_{\rm ff}$ is the free-fall timescale. Here, $t_{\rm ff}$ can be obtained given the enclosed mass, M, within a radius R, namely,

$$t_{\rm ff} = \sqrt{\frac{R^3}{GM}}. \quad (2)$$

By measuring the proper motion, Diaz-Rodriguez et al. (2022) derive a total mass of VLA4A/B as 1 $M_\odot$ from the orbital motion. Given the detected farthest projected distance of the DCN streamer ~700 au, we derived a free-fall time of ~3000 yr. We note that this can be taken as an upper limit since the initial velocity of DCN is ignored in the calculation (Valdivia-Mena et al. 2022). As a result, we find a mass infalling rate of $\geq 1.4 \times 10^{-6}\ M_\odot\ {\rm yr}^{-1}$ if this streamer is in a free-fall motion. This value is similar to that of the streamers found in other Class I protostars (Per-emb-2: $10^{-6}\ M_\odot\ {\rm yr}^{-1}$ Pineda et al. 2020; Per-emb-50: $1.3 \times 10^{-6}\ M_\odot\ {\rm yr}^{-1}$ Valdivia-Mena et al. 2022). The infalling streamer appears to connect to the bursting source VLA4A from the ALMA high-resolution continuum image (Diaz-Rodriguez et al. 2022), for which the circumstellar disk has a mass of 0.004–0.009 $M_\odot$. It would take less than 2800–6400 yr for the infalling streamer to replenish this disk. If the streamer supplies the material to the circumbinary disk with $M_{\rm disk} = 0.052\ M_\odot$, a replenishment could happen in a timescale of <37 000 yr. These timescales are broadly consistent with the recurrence timescale of 10^3–10^5 yr for accretion bursts (Scholz et al. 2013; Contreras Peña et al. 2019; Fischer et al. 2019; Hsieh et al. 2018, 2019; Park et al. 2021), for which the timescale is believed to be smaller in earlier stages.

The high luminosity ($L \sim 45.3\ L_\odot$) of SVS13A suggests that it is undergoing an accretion burst with a protostellar mass accretion rate of $2.8 \times 10^{-5}\ M_\odot\ {\rm yr}^{-1}$ (Hsieh et al. 2019). As a result, the infalling rate from the envelope to the disk contributed via the streamer can be ≥5% of the protostellar mass accretion rate. If we assume the streamer dominates the mass infalling rate and the disk mass is constant, this implies that the protostar spends >5% of the time in the burst phase, that is, "duty cycle" in episodic accretion (Audard et al. 2014). However, if a significant mass is accreted onto the central source during the quiescent phase, this will reduce this value. For comparison, by modeling the luminosity distribution, Evans et al. (2009) derived a duty cycle of 7% and Dunham & Vorobyov (2012) estimate a value of 1.3%. We note that SVS13A appears to be a binary system (or perhaps triple, Lefèvre et al. 2017) and it is still unclear if the infalling streamer is feeding directly the disk around VLA4A or the circumbinary disk without higher-resolution observations.

4.3. Structure of SVS13A

The origin of the COMs in star-forming regions is not fully understood at present. These molecules are typically found to trace inner compact regions, where the temperature is higher than ~100 K. These regions are called hot corinos in low-mass star-forming regions (Ceccarelli 2004). However, COMs can also be present in the shocked gas near the centrifugal barrier (Csengeri et al. 2018) and irradiated cavity walls of outflows (Drozdovskaya et al. 2015). SVS13A contains a central binary (VLA4A and VLA4B), circumbinary disk, and a few spiral features (Fig. 1, also see Diaz-Rodriguez et al. 2022). Furthermore, the presence of infalling streamers has been suggested to produce shocked gas, enriching the chemistry (Bianchi et al. 2022b) and causing the increase of velocity dispersion (Diaz-Rodriguez et al. 2022) in VLA4A. Toward SVS13A, the close binary with the spiral structure seen in continuum emission was considered to be a fragmenting disk due to gravitational instability (Tobin et al. 2018). However, through DCN emission, we find that the spiral is connected to an infalling streamer that extends to an outer region (~700 au) of the protostellar envelope. Although the size of the CH_3CN emitting region (0.″27, Table 1) is comparable to the size of VLA4A's circumstellar disk (~0.″23 in diameter, Diaz-Rodriguez et al. 2022), the CH_3CN line profile (position 1 in Fig. 6) suggests that the emission does not only come from a single component. The two-component model further supports this hypothesis; the CH_3CN emission, at different velocities, originates from regions with different column densities and temperatures (or H_2 density). In the two-component model, the blueshifted component dominates the line emission and has a velocity relatively close to the rotating envelope or disk surrounding VLA4A ($V_{\rm lsr} = 7.36\ {\rm km\ s^{-1}}$) seen via aGg'-$(CH_2OH)_2$ by Diaz-Rodriguez et al. (2022). This also corresponds to the velocity of the DCN and $C^{18}O$ streamer at the landing site, suggesting that the accretion from the large scale affects the circumstellar material. On the other hand, the optically thick component at the redshifted side is not present in the aGg'-$(CH_2OH)_2$ line. One possibility is that it comes from the presumed primary VLA4B ($V_{\rm lsr} = 9.33\ {\rm km\ s^{-1}}$). Kinematically, the central positions of the CH_3CN K = 3 and K = 7 emission at different velocities also reveal a velocity structure that cannot be explained by a simple rotationally supported disk (Figs. 3 and B.1). Therefore, we suggest that CH_3CN as a COM not only traces disk material, but is also affected by the large-scale infall of material provided by the streamer. This scenario is also proposed by Bianchi et al. (2022b) based on the elongated COM emission toward both VLA4A/4B. Supporting this scenario, in the case of the close Class 0 binary IRAS 16293-2422 A, the COM emission was resolved down to a scale of 10 au, and displayed several peaks outside the individual compact disks (Maureira et al. 2020). These peaks, located at about 30 au from the protostars, presumably trace shocks related to the accretion

of the circumbinary material into the individual Keplerian disks (Mösta et al. 2019; Maureira et al. 2020).

We find the large-scale infalling streamer funneling material to the protostellar system. The infalling streamer seen via DCN, $C^{18}O$ and continuum emission lands closer to VLA4A (both spatially and spectrally), the source undergoing an accretion burst. For example, toward the binary system [BHB2007] 11A, Alves et al. (2019) find a filamentary structure that connects the central binary system to the circumbinary disk. However, at the current spatial resolution, it is unclear if the infalling streamer in SVS13A lands on the disk surrounding VLA4A or the circumbinary disk. A higher resolution observation is required to disentangle the complex structure in the central region.

5. Conclusion

We present CH_3CN (12_K–11_K), $CH_3{}^{13}CN$ ($12_K - 11_K$), DCN (3–2), and $C^{18}O$ (2–1) observations toward SVS13A (Per-emb-44) from the NOEMA PRODIGE Large Program. Through the line emission, we study the dynamics and physical conditions of the system. Our main conclusions are summarized as follows:

1. Through MCMC modeling, we find a low $CH_3CN/CH_3{}^{13}CN$ ratio of 16, which is much lower than the isotope ratio value. We suggest that the simple one-velocity component assumption is affected severely by optical depth, especially in a complex structure as SVS13A. Properly measuring the column density requires data including multiple transitions with different optical depths and high spatial and spectral resolution to decompose the line emission;
2. The CH_3CN line profile is better explained by a two-component velocity model. By splitting it into two components, we find CH_3CN can trace regions with dramatic differences in density and/or temperature. The kinematics show that the CH_3CN emission can be affected by the infalling material from a streamer connecting the protostellar system to the outer envelope;
3. Contrary to the previous interpretation, namely, that the spiral seen via the continuum emission is part of a gravitationally unstable disk, we find that it is in fact connected to a much larger feature. A streamer, possibly infalling, with a length of ~700 au is identified; it is partially seen through multiple tracers, including DCN, $C^{18}O$, and continuum emission. Under the assumption that the streamer is infalling, it contributes a mass infalling rate onto the protostellar system of $\geq 1.4 \times 10^{-6}\ M_\odot\ \mathrm{yr}^{-1}$, ≥5% of the current protostellar mass accretion rate, $2.8 \times 10^{-5}\ M_\odot\ \mathrm{yr}^{-1}$. VLA4A might spend ~5% of time in the bursting phase of episodic accretion.

Our results show that the CH_3CN and $CH_3{}^{13}CN$ emission traces hot gas in a complex structure in SVS13A. This region is connected to a streamer with a length of ~700 au. If this streamer is feeding the central protobinary system, it can contribute to a significant mass-accretion rate. We speculate that the complexity might be caused by or associated with the large-scale streamer. Observations with a higher spatial resolution are required to disentangle it.

Acknowledgements. We are grateful for the anonymous referee for the thorough and insightful comments that helped to improve this paper significantly. The authors thank Dr. Emmanuel Caux, Dr. Valerio Lattanzi, Dr. Silvia Spezzano, and Dr. Christian Endres for valuable discussion in the line analyzing using CASSIS and CDMS. T.-H.H., D.S.-C., J.E.P., P.C., M.T.V, and M.J.M. acknowledge the support by the Max Planck Society. D.S.-C. is supported by an NSF Astronomy and Astrophysics Postdoctoral Fellowship under award AST-2102405. A.L.S. acknowledges support from the European Union's Horizon 2020 research and innovation program under the Marie SkłodowskaCurie grant agreement no. 811312 for the Project "Astro-Chemical Origin" (ACO). A.F. acknowledges Spanish MICIN for funding support from PID2019-106235GB-I00. N.C. acknowledges funding from the European Research Council (ERC) via the ERC Synergy Grant ECOGAL (grant 855130), and from the French Agence Nationale de la Recherche (ANR) through the project COSMHIC (ANR-20- CE31-0009). M.T. acknowledges partial support from project PID2019-108765GB-I00 funded by MCIN/AEI/10.13039/501100011033. This work is based on observations carried out under project number L19MB with the IRAM NOEMA Interferometer. IRAM is supported by INSU/CNRS (France), MPG (Germany) and IGN (Spain). This paper makes use of the following ALMA data: ADS/JAO.ALMA#2013.1.00031.S. ALMA is a partnership of ESO (representing its member states), NSF (USA) and NINS (Japan), together with NRC (Canada), MOST and ASIAA (Taiwan), and KASI (Republic of Korea), in cooperation with the Republic of Chile. The Joint ALMA Observatory is operated by ESO, AUI/NRAO and NAOJ.

References

Alves, F. O., Caselli, P., Girart, J. M., et al. 2019, Science, 366, 90
Alves, F. O., Cleeves, L. I., Girart, J. M., et al. 2020, ApJ, 904, L6
Anglada, G., Rodríguez, L. F., & Torrelles, J. M. 2000, ApJ, 542, L123
Anglada, G., Rodríguez, L. F., Osorio, M., et al. 2004, ApJ, 605, L137
Armitage, P. J., Livio, M., & Pringle, J. E. 2001, MNRAS, 324, 705
Astropy Collaboration (Robitaille, T. P., et al.) 2013, A&A, 558, A33
Audard, M., Ábrahám, P., Dunham, M. M., et al. 2014, Protostars and Planets VI, 387
Belloche, A., Maury, A. J., Maret, S., et al. 2020, A&A, 635, A198
Beltrán, M. T., Cesaroni, R., Neri, R., et al. 2011, A&A, 525, A151
Bergner, J. B., Guzmán, V. G., Öberg, K. I., et al. 2018, ApJ, 857, 69
Bisschop, S. E., Jørgensen, J. K., Bourke, T. L., et al. 2008, A&A, 488, 959
Bianchi, E., Codella, C., Ceccarelli, C., et al. 2017, MNRAS, 467, 3011
Bianchi, E., Codella, C., Ceccarelli, C., et al. 2019, MNRAS, 483, 1850
Bianchi, E., Ceccarelli, C., Codella, C., et al. 2022a, A&A, 662, A103
Bianchi, E., López-Sepulcre, A., Ceccarelli, C., et al. 2022, ApJ, 928, L3
Bockelée-Morvan, D., & Biver, N. 2017, Philos. Trans. Roy. Soc. Lond. A, 375, 20160252
Bottinelli, S., Ceccarelli, C., Williams, J. P., et al. 2007, A&A, 463, 601
Brünken, S., Fuchs, U., Lewen, F., et al. 2004, J. Mol. Spectrosc., 225, 152
Cabedo, V., Maury, A., Girart, J. M., et al. 2021, A&A, 653, A166
Calcutt, H., Jørgensen, J. K., Müller, H. S. P., et al. 2018, A&A, 616, A90
Caselli, P., & Ceccarelli, C. 2012, A&AR, 20, 56
Ceccarelli, C. 2004, Star Formation in the Interstellar Medium: In Honor of David Hollenbach, 323, 195
Choudhury, S., Pineda, J. E., Caselli, P., et al. 2020, A&A, 640, A6
Contreras Peña, C., Naylor, T., & Morrell, S. 2019, MNRAS, 486, 4590
Codella, C., Ceccarelli, C., Bianchi, E., et al. 2016, MNRAS, 462, L75
Codella, C., Bianchi, E., Podio, L., et al. 2021, A&A, 654, A52
Csengeri, T., Bontemps, S., Wyrowski, F., et al. 2018, A&A, 617, A89
De Simone, M., Codella, C., Testi, L., et al. 2017, A&A, 599, A121
Diaz-Rodriguez, A. K., Anglada, G., Blázquez-Calero, G., et al. 2022, ApJ, 930, 91
Drozdovskaya, M. N., Walsh, C., Visser, R., et al. 2015, MNRAS, 451, 3836
Dunham, M. M., & Vorobyov, E. I. 2012, ApJ, 747, 52
Endres, C. P., Schlemmer, S., Schilke, P., et al. 2016, J. Mol. Spectrosc., 327, 95
Evans, N. J., Dunham, M. M., Jørgensen, J. K., et al. 2009, ApJS, 181, 321
Fischer, W. J., Safron, E., & Megeath, S. T. 2019, ApJ, 872, 183
Garufi, A., Dominik, C., Ginski, C., et al. 2022, A&A, 658, A137
Galván-Madrid, R., Zhang, Q., Keto, E., et al. 2010, ApJ, 725, 17
Ginsburg, A., & Mirocha, J. 2011, Astrophysics Source Code Library, [ascl:1109.001]
Ginski, C., Facchini, S., Huang, J., et al. 2021, ApJ, 908, L25
Goldreich, P., & Kwan, J. 1974, ApJ, 189, 441
Green, S. 1986, ApJ, 309, 331
Harsono, D., Visser, R., Bruderer, S., et al. 2013, A&A, 555, A45
Herbst, E., & van Dishoeck, E. F. 2009, ARA&A, 47, 427
Hogg, D. W., & Foreman-Mackey, D. 2018, ApJS, 236, 11
Hsieh, T.-H., Murillo, N. M., Belloche, A., et al. 2018, ApJ, 854, 15
Hsieh, T.-H., Murillo, N. M., Belloche, A., et al. 2019, ApJ, 884, 149
Hunter, J. D. 2007, Comput. Sci. Eng., 9, 90
Hunter, T. R., Brogan, C. L., Cyganowski, C. J., et al. 2014, ApJ, 788, 187
Ilee, J. D., Cyganowski, C. J., Nazari, P., et al. 2016, MNRAS, 462, 4386
Kristensen, L. E., van Dishoeck, E. F., Bergin, E. A., et al. 2012, A&A, 542, A8
Lefèvre, C., Cabrit, S., Maury, A. J., et al. 2017, A&A, 604, L1
Lee, K. I., Dunham, M. M., Myers, P. C., et al. 2016, ApJ, 820, L2
Loomis, R. A., Cleeves, L. I., Öberg, K. I., et al. 2018, ApJ, 859, 131

Mangum, J. G., & Shirley, Y. L. 2015, PASP, 127, 266
Maureira, M. J., Pineda, J. E., Segura-Cox, D. M., et al. 2020, ApJ, 897, 59
McMullin, J. P., Waters, B., Schiebel, D., et al. 2007, Astronomical Data Analysis Software and Systems XVI, 376, 127
Milam, S. N., Savage, C., Brewster, M. A., et al. 2005, ApJ, 634, 1126
Miotello, A., Bruderer, S., & van Dishoeck, E. F. 2014, A&A, 572, A96
Möller, T., Endres, C., & Schilke, P. 2017, A&A, 598, A7
Mösta, P., Taam, R. E., & Duffell, P. C. 2019, ApJ, 875, L21
Müller, H. S. P., Schlöder, F., Stutzki, J., et al. 2005, J. Mol. Struct., 742, 215
Müller, H. S. P., Drouin, B. J., & Pearson, J. C. 2009, A&A, 506, 1487
Müller, H. S. P., Brown, L. R., Drouin, B. J., et al. 2015, J. Mol. Spectrosc,, 312, 22
Mumma, M. J., & Charnley, S. B. 2011, ARA&A, 49, 471
Murillo, N. M., van Dishoeck, E. F., Hacar, A., et al. 2022, A&A, 658, A53
Ortiz-León, G. N., Loinard, L., Dzib, S. A., et al. 2018, ApJ, 869, L33
Park, W., Lee, J.-E., Contreras Peña, C., et al. 2021, ApJ, 920, 132
Pineda, J. E., Segura-Cox, D., Caselli, P., et al. 2020, Nat. Astron., 4, 1158
Pineda, J. E., Arzoumanian, D., André, P., et al. 2022 ArXiv e-prints [arXiv:2205.03935]
Robitaille, T. & Bressert, E. 2012, Astrophysics Source Code Library, [ascl:1208.017]
Roueff, E., Loison, J. C., & Hickson, K. M. 2015, A&A, 576, A99
Rubin, M., Altwegg, K., Balsiger, H., et al. 2019, MNRAS, 489, 594
Sargent, A. I. & Beckwith, S. 1987, ApJ, 323, 294
Scholz, A., Froebrich, D., & Wood, K. 2013, MNRAS, 430, 2910
Seifried, D., & Walch, S. 2015, MNRAS, 452, 2410
Seifried, D., Banerjee, R., Pudritz, R. E., et al. 2015, MNRAS, 446, 2776
Segura-Cox, D. M., Looney, L. W., Tobin, J. J., et al. 2018, ApJ, 866, 161
Shirley, Y. L. 2015, PASP, 127, 299
Smirnov-Pinchukov, G. V., Semenov, D. A., Akimkin, V. V., et al. 2020, A&A, 644, A4
Stephens, I. W., Dunham, M. M., Myers, P. C., et al. 2018, ApJS, 237, 22
Thieme, T. J., Lai, S.-P., Lin, S.-J., et al. 2022, ApJ, 925, 32
Tobin, J. J., Looney, L. W., Li, Z.-Y., et al. 2016, ApJ, 818, 73
Tobin, J. J., Looney, L. W., Li, Z.-Y., et al. 2018, ApJ, 867, 43
Tychoniec, Ł., Tobin, J. J., Karska, A., et al. 2018, ApJS, 238, 19
Tychoniec, Ł., Manara, C. F., Rosotti, G. P., et al. 2020, A&A, 640, A19
Valdivia-Mena, M. T., Pineda, J. E., Segura-Cox, D. M., et al. 2022, A&A, 667, A12
van der Tak, F. F. S., Black, J. H., Schöier, F. L., et al. 2007, A&A, 468, 627
van der Tak, F. F. S., Lique, F., Faure, A., et al. 2020, Atoms, 8, 15
Van Der Walt, S., Colbert, S. C., & Varoquaux, G. 2011, Computing in Science & Engineering, 13, 22
van Dishoeck, E. F. 2014, Faraday Discuss., 168, 9
Vastel, C., Bottinelli, S., Caux, E., et al. 2015, SF2A-2015: Proceedings of he Annual meeting of the French Society of Astronomy and Astrophysics, 313
Virtanen, P., Gommers, R., Oliphant, et al. (2020). SciPy 1.0: Fundamental Algorithms for Scientific Computing in Python. Nature Methods
Vorobyov, E. I., & Basu, S. 2010, ApJ, 719, 1896
Wilson, T. L., & Rood, R. 1994, ARA&A, 32, 191
Yang, Y.-L., Sakai, N., Zhang, Y., et al. 2021, ApJ, 910, 20
Yoshida, T. C., Nomura, H., Furuya, K., et al. 2022, ApJ, 932, 126
Zhao, B., Caselli, P., Li, Z.-Y., et al. 2018, MNRAS, 473, 4868

Appendix A: MCMC fitting to CH_3CN/$CH_3{}^{13}CN$ spectrum

We conducted an MCMC fitting to the CH_3CN and $CH_3{}^{13}CN$ spectrum using CASSIS (Vastel et al. 2015). The information behind the Markov chain for each model is listed in Table A.1. The same process is applied for each of these four models, and here we show the plots for the LTE one-velocity-component model as an example. Long Markov chains are taken in order to better sample the parameter space. We use trace plot and autocorrelation time to test the convergence (Figures A.1 and A.2); however, we note that these tests are only heuristic indicators of convergence (Hogg & Foreman-Mackey 2018). The χ^2 and acceptance rate as functions of step are plotted with trace plots. The acceptance rate is from the number of the accepted and rejected proposals from the random walker (or Markov chain). The recommanded value is 0.2–0.5 and 0.234 for best-performance in high-dimensional problems (Hogg & Foreman-Mackey 2018). The autocorrelation time at lags is estimated using the Python Package statsmodels[6]. We compare the estimated autocorrelation time $\tau_{\rm estimate}$ with different sample sizes. The autocorrelation time indicates a sequence within which the sampling points are similar. In other words, two sampled points with a separation $> \tau_{\rm estimate}$ are considered to be independent. We find that $\tau_{\rm estimate}$ had become stable in larger sample sizes in our chain (Figure A.2). The trace plots and autocorrelation time also act as a guide for tuning the steps of the walkers for each parameter. The step sizes are thus tuned to be comparable to the dispersion of the sample, and keep an acceptance rate between 0.2-0.5. For each model, this procedure is repeated several times until a proper tuning is found. We checked the trace plots (as well as the χ^2 derived by CASSIS) and removed the beginning of the chain (burn-in phase; 1500-15000 steps depending on models). To obtain independent points from the sample, we take one data point every $\tau_{\rm int}/2$ sample, i.e., thinning process; while the $\tau_{\rm int}$ can be very different among the fitting parameters (Table A.1), here we take 1/2 of the smallest $\tau_{\rm int}$ in order to preserve a large sample (Table 1). The physical parameters and their uncertainties are thus estimated using these thinning samples. Finally, the best fit of the four models is shown in Figures A.3 to A.6. The opacities of the CH_3CN K-ladder transitions for each component from the four best-fit models are listed in Table A.2. The corner plot for the one velocity component model is shown in Figure A.7

Appendix B: Kinematic models

In order to probe the origin of the CH_3CN emission in SVS13A, we compared the kinematic models with the three disks from Diaz-Rodriguez et al. (2022), that is, the circumstellar disks of VLA4A, VLA4B as well as the circumbinary disk (Figure B.1). The emitting position at each velocity is obtained by Gaussian fitting in uv-space (Figure 3). Using the central position, position angle, and inclination angle of the VLA4A, VLA4B disks, and the circumbinary disk from Diaz-Rodriguez et al. (2022), we derived the de-projected radius of the CH_3CN emission from the Gaussian position. Then, we plotted the measured and modeled velocities of the CH_3CN emission corresponding to these three disks. Comparing the line-of-sight velocity of a Keplerian model, the CH_3CN emission seems to trace part of a disk of VLA4A (see the top panel of Figure B.1). However, at least at the current spatial resolution, we find that the rotation curve cannot be simply interpreted by a simple slope for Keplerian motion, $V \propto r^{-0.5}$, or conservation of angular momentum (infalling disk), $V \propto r^{-1}$ (see Figure B.1).

[6] https://www.statsmodels.org/stable/index.html

Appendix C: Channel maps

Figure C.1 shows the channel maps from 7.22 to 10.16 km s^{-1}. The full channel map shows that in addition to the infalling streamer, DCN actually traces more extended gas components. At low velocities ~7.4 – 8.0 km s^{-1}, DCN traces a gas component offset from the continuum streamer, which is also seen in the $C^{18}O$ emission (Figure 7). At ~8.26 – 8.95 km s^{-1}, the DCN emission is dominated by the infalling streamer. The redshifted emission >9 km s^{-1} is likely associated with another extended component.

The $C^{18}O$ blueshifted component is found to spatially match the inner part of the spiral or streamer seen in the continuum emission (Tobin et al. 2018). Figure C.2 shows the channel maps of this blueshifted component. The $C^{18}O$ emission at this velocity range 7.50 – 8.25 km s^{-1} is consistent with the velocity map of the DCN blueshifted component (Figure D.1) and spatially matches the continuum spiral well.

Appendix D: Decomposition of DCN (3-2) spectra

We conducted an HFS fitting in the DCN (3-2) channel map. Three different velocity components are found (Figure D.1). The fitting is firstly conducted with one, two, and three velocity components. To proceed with the fitting, we took several boundary constraints in the three components; blueshifted component: $V_{\rm lsr} < 8.8$ km s^{-1} and $\sigma < 0.6$ km s^{-1}, redshifted component: $V_{\rm lsr} > 8.8$ km s^{-1} and $\sigma < 0.6$ km s^{-1}, and broad component: $\sigma < 2$ km s^{-1}.

For each pixel, we selected the model with one, two or three velocity components based on the Akaike information criterion (AIC),

$$AIC = 2\mathrm{k} + \chi^2 + C, \tag{D.1}$$

where k is the degree of freedom (3, 6, and 9), χ^2 is obtained from the fitting residual, and C is a constant (see Appendix E. in Choudhury et al. 2020). Comparing the AIC in each pixel, we used the model with the lowest AIC value.

Table A.1. MCMC fitting

Model	draws	chain length	$\tau_{\rm int}$	thinned sample
LTE model	10^6	390513	45-398	17737
LTE split iso.	10^6	294053	62-2057	9465
LTE 2-comp	2×10^6	397485	204-1191	3888
non-LTE 2-comp	10^6	234956	466-1665	1001

Table A.2. Opacities of best-fit CH_3CN model

Model	component	K0	K1	K2	K3	K4	K5	K6	K7	
LTE model	-	2.21	2.13	1.92	3.20	1.24	0.89	1.18	0.36	
LTE two species	CH_3CN		2.23	2.15	1.93	3.21	1.24	0.89	1.17	0.35
	$CH_3{}^{13}CN$	0.21	0.20	0.17	0.27	0.09	0.06	-	-	
LTE 2-comp	extend	2.73	2.61	2.28	3.64	1.33	0.88	1.06	0.28	
	compact	4.32	4.18	3.78	6.41	2.54	1.87	2.55	0.80	
non-LTE 2-comp	extend	2.82	2.51	2.30	3.75	1.45	0.96	1.41	0.33	
	compact	13.35	11.79	10.52	1.73	6.07	3.88	5.10	1.22	

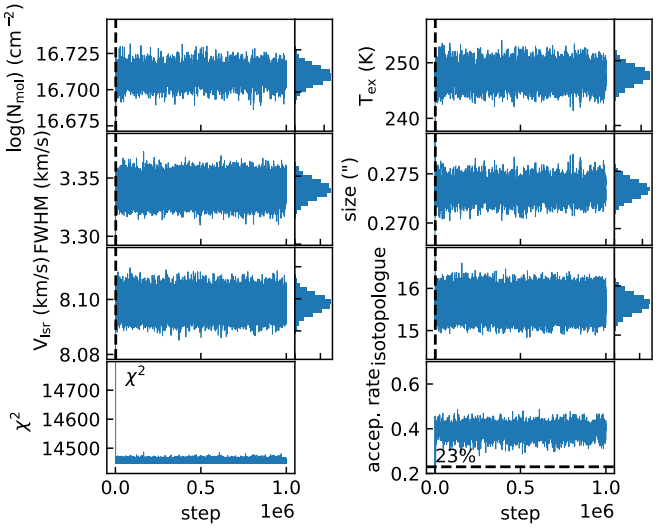

Fig. A.1. Trace plot of the MCMC fitting for the LTE 1-component model. Each panel is for one physical parameter, for which the panel "isotopologue" is the column density ratio $\frac{CH_3CN}{CH_3{}^{13}CN}$. The vertical dashed line represents the cut before which the data points are discarded and the histogram in the right is plotted based on the saved sample. The bottom panels show the χ^2 derived by CASSIS and acceptance rate measured in every 300 steps.

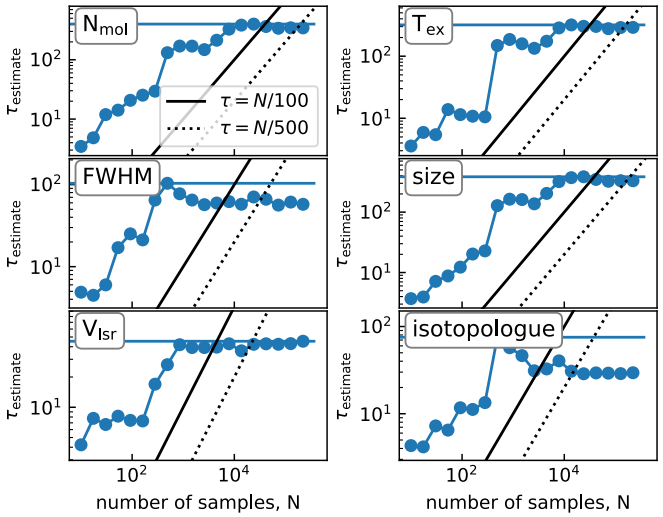

Fig. A.2. Autocorrelation time as a function of number of samples for estimation for the LTE 1-component model in the MCMC fitting. The horizontal line represents the maximal autocorrelation time (τ), and the solid and dashed lines represent the number of sample with 50 and 500 times of τ.

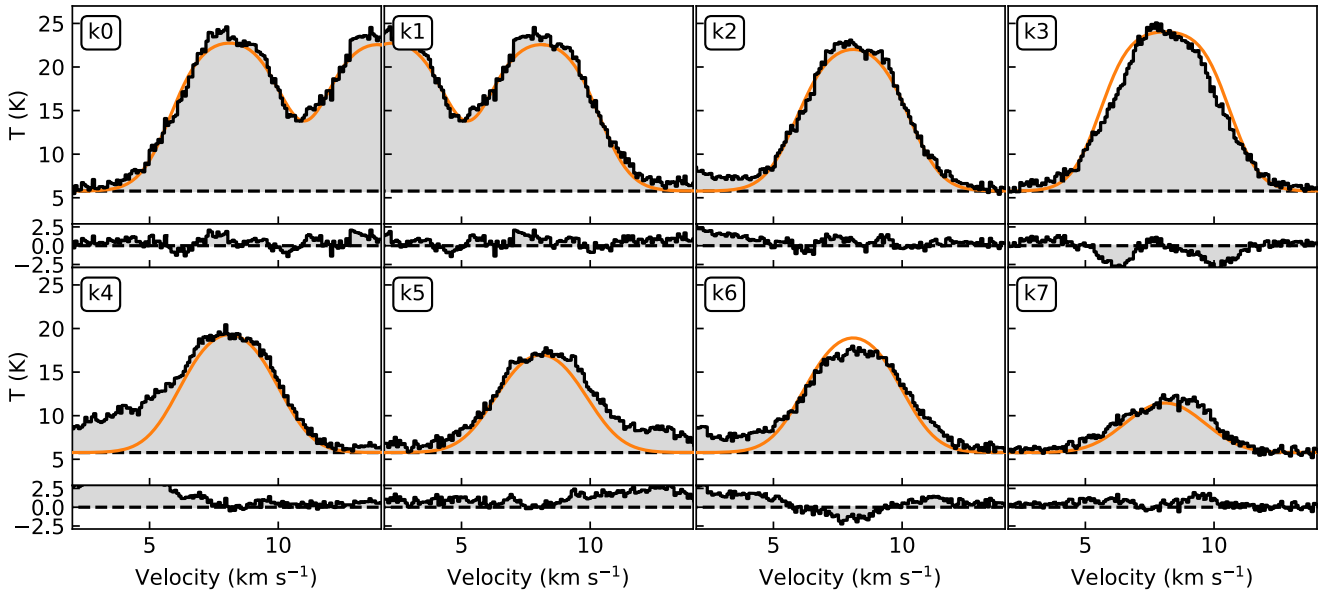

Fig. A.3. Zoom-in spectra for each K-ladder component of CH_3CN J=12-11. The orange curve shows the best-fit one-component LTE model. The bottom frame in each panel shows the residual from the fitting.

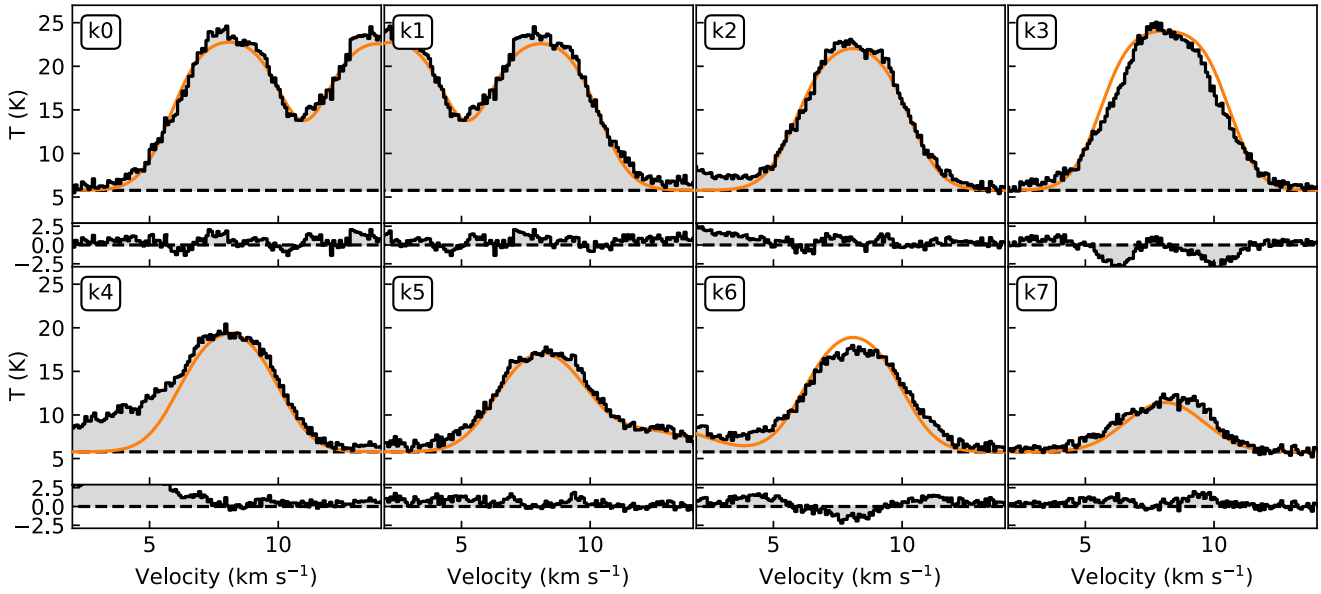

Fig. A.4. Zoom-in spectra for each K-ladder component of CH_3CN J=12-11. The orange curve shows the best-fit LTE model considering CH_3CN and $CH_3{}^{13}CN$ as two species. The bottom frame in each panel shows the residual from the fitting.

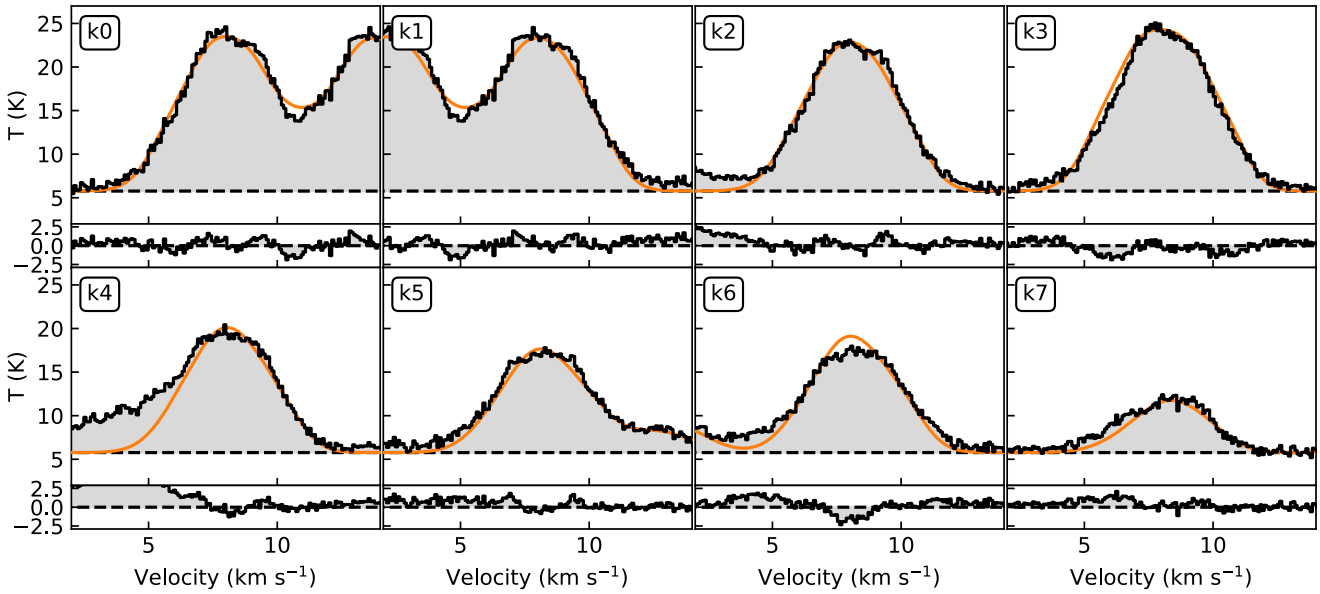

Fig. A.5. Zoom-in spectra for each K-ladder component of CH_3CN J=12-11. The orange curve shows the best-fit two-component LTE model. The bottom frame in each panel shows the residual from the fitting.

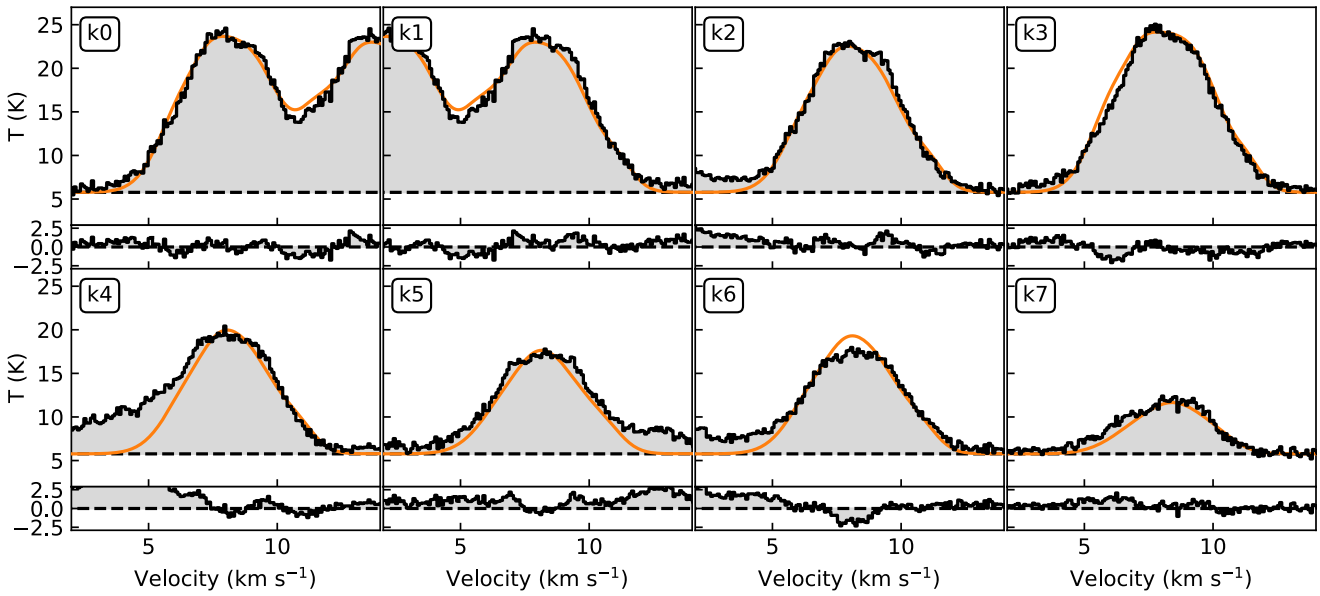

Fig. A.6. Zoom-in spectra for each K-ladder component of CH_3CN J=12-11. The orange curve shows the best-fit two-component non-LTE model. The bottom frame in each panel shows the residual from the fitting.

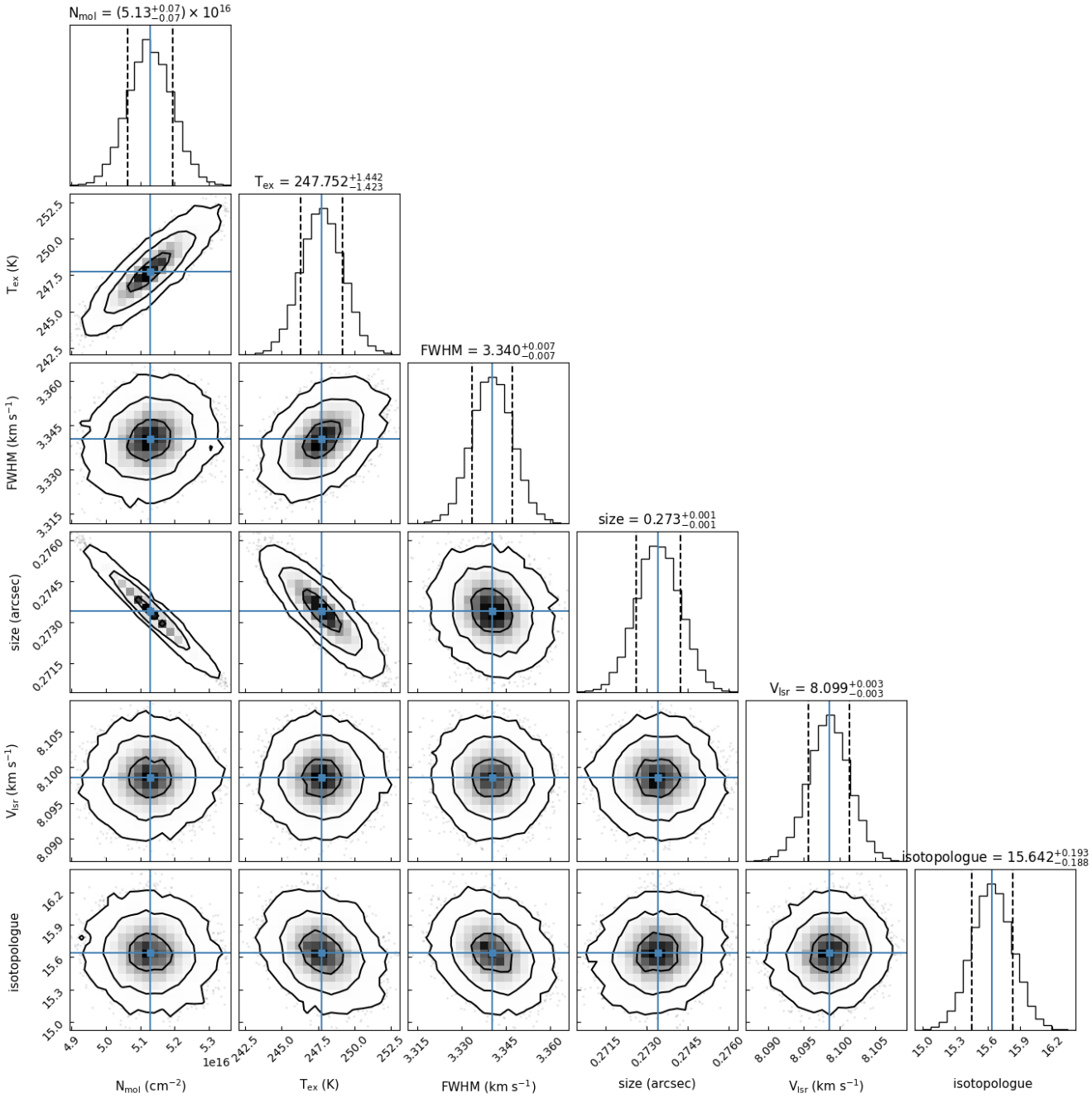

Fig. A.7. Corner plot of the one-component MCMC fitting. The parameters from left to right are CH_3CN column density, excitation temperature, FWHM line width, source size, systemic velocity, and isotopologue ratio $\frac{CH_3CN}{CH_3{}^{13}CN}$.

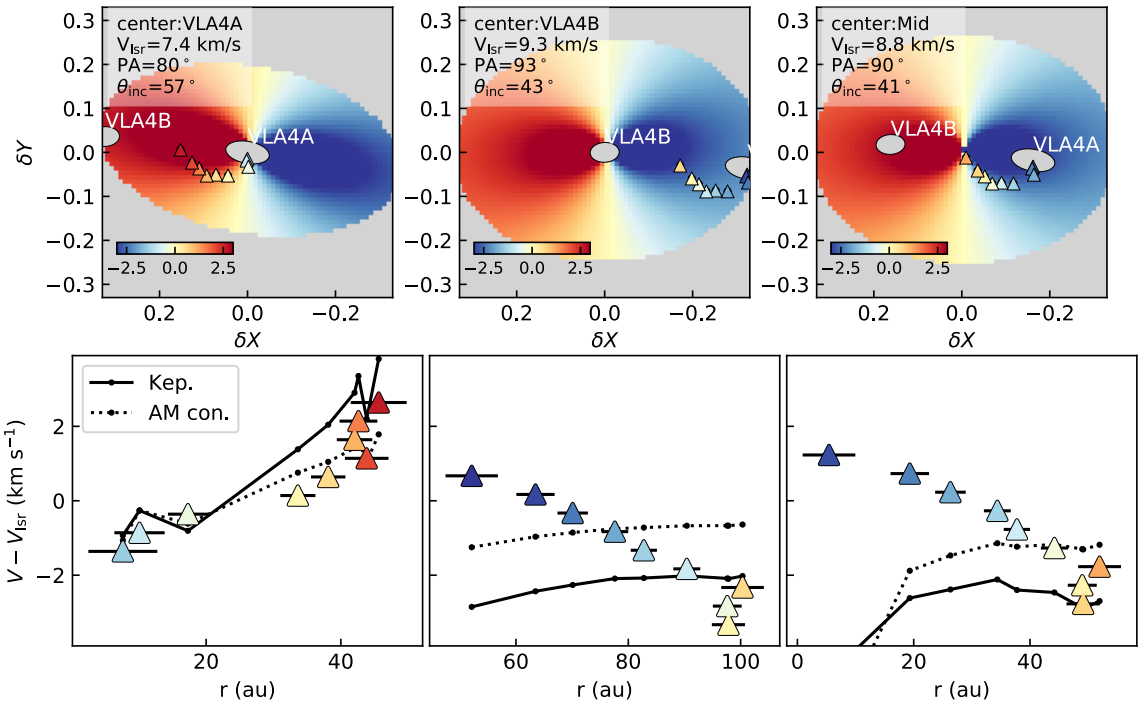

Fig. B.1. Gaussian centers of CH_3CN $12_3 - 11_3$ emission at different velocities from the uv-domain fitting in comparison with the line-of-sight velocity of a Keplerian disk model ($V \propto r^{-0.5}$), shown at the top. These models adopte three sets of V_{lsr}, PA, θ_{inc} listed in the upper-left corner from Diaz-Rodriguez et al. (2022) for VLA4A/B circumstellar disks and the circumbinary disk. Line-of-sight velocities of these points as a function of the inclination-corrected radius, shown at the bottom. The solid and dotted lines show modeled velocities at the corresponding emitting positions assuming Keplerian motion ($V \propto r^{-0.5}$) and conservation of angular momentum ($V \propto r^{-1}$), respectively. We note that the modeled curves will only shift vertically if the velocity of the model is scaled.

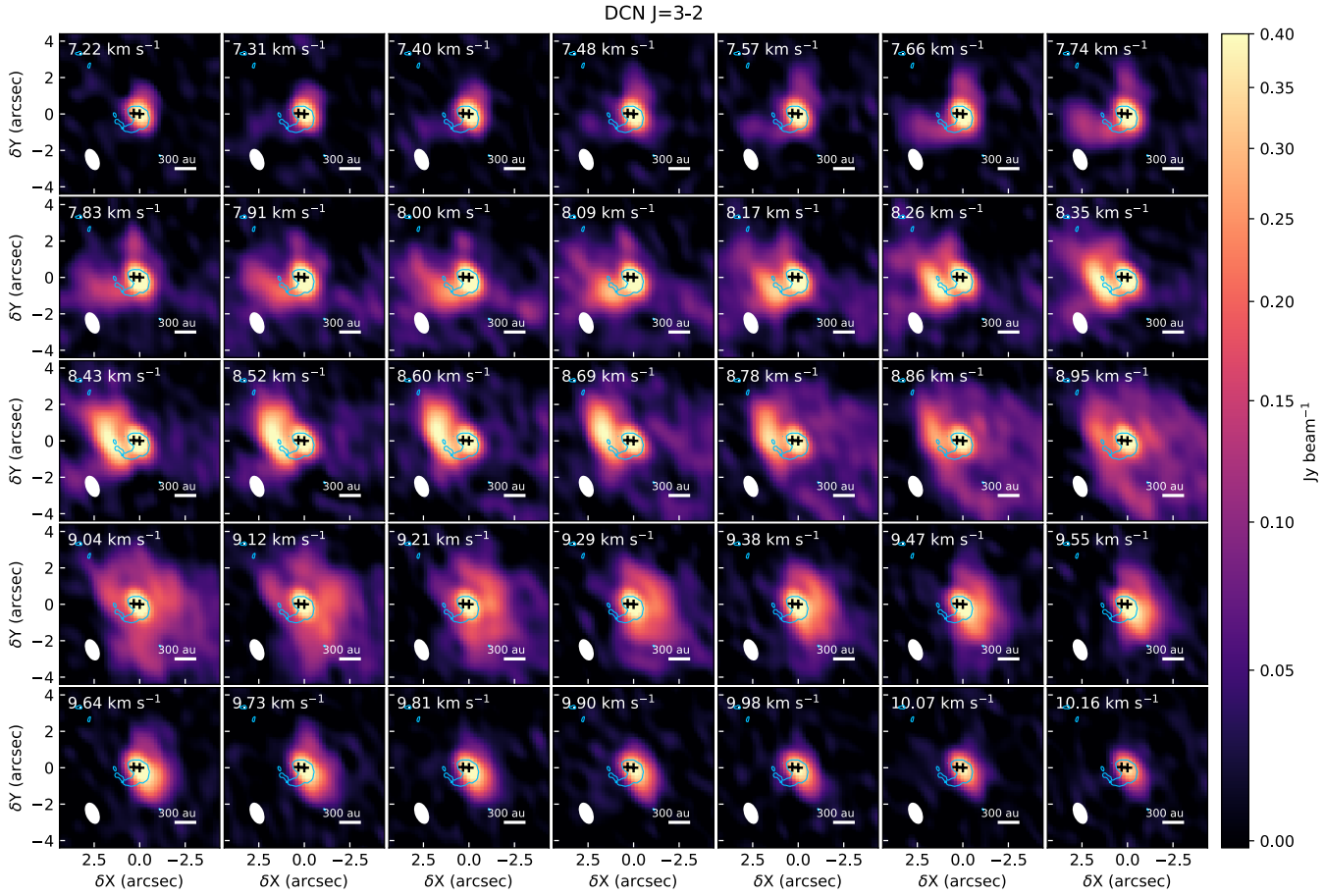

Fig. C.1. DCN (3-2) channel map. The blue contour shows the ALMA continuum emission at 3σ.

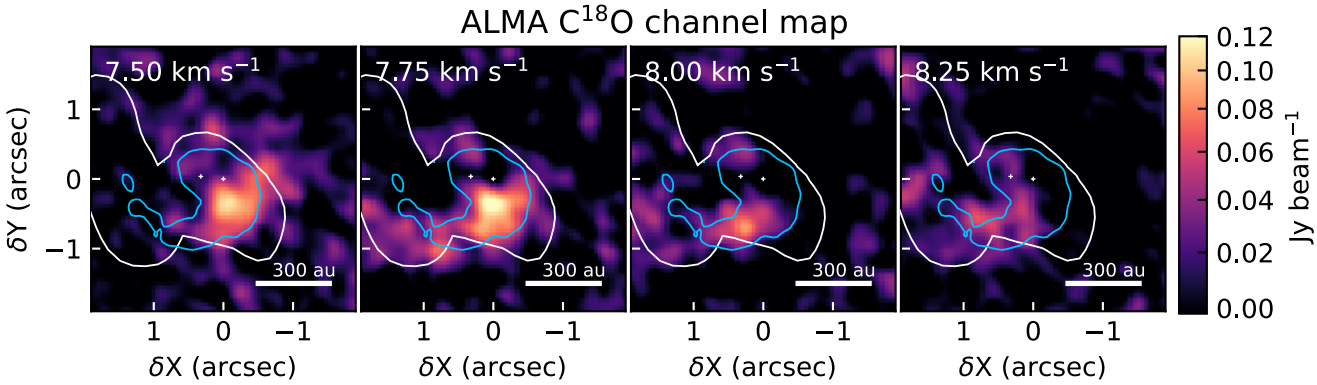

Fig. C.2. ALMA $C^{18}O$ channel map. The blue contour shows the ALMA continuum emission at 3σ and the white contour shows the DCN (3-2) peak intensity map at 25σ.

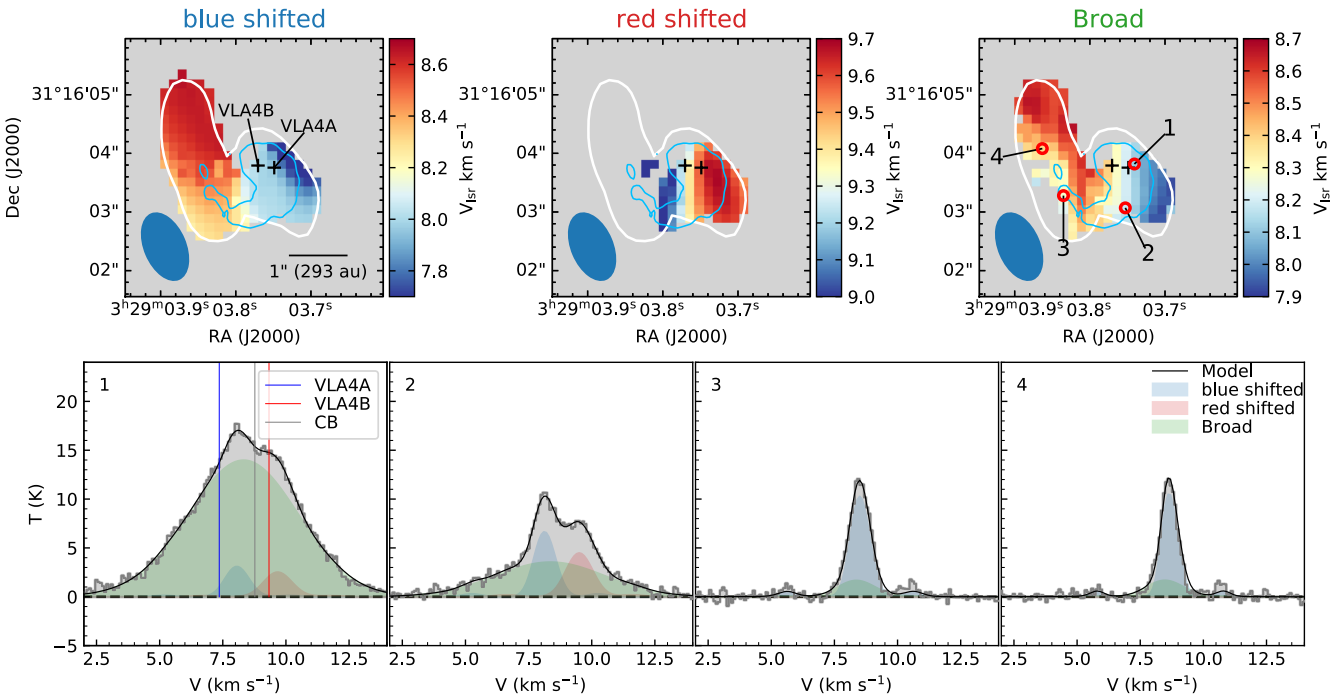

Fig. D.1. DCN (3-2) centroid-velocity maps of the three velocity components from the hyperfine structure fitting, shown at the top. The white contour shows the peak intensity above 25σ. The blue contour shows the ALMA 1.3 mm continuum emission at the 3σ level. Below, we have the spectra of DCN (3-2) with the hyperfine structure fitting toward the four positions marked in the top right panel. The three vertical lines represent the systemic velocites of VLA4A, VLA4B, and the circumbinary disk from Diaz-Rodriguez et al. (2022).